Time-dependent approach to the continuum shell model

Alexander Volya
Department of Physics, Florida State University, Tallahassee, Florida 32306-4350, USA
(Received 20 November 2008; published 14 April 2009)

The continuum shell model represents a merger of the traditional shell model, the tool for understanding nuclear structure, with the physics of reactions. In this work a new time-dependent approach to the continuum shell model is presented, where construction and application of the time-dependent evolution operator culminate in an effective and successful strategy for tackling the nonstationary many-body dynamics. Details behind the technique and methods to overcome general problems associated with quantum many-body physics on the verge of stability are discussed. Topics presented include the construction of the time-dependent Green's function, the full propagator from the exact solution of Dyson's equation, a treatment of decays and virtual self-energy terms, the explicit time dependence and survival probability of states, the strength function and collective features of unstable systems, the center-of-mass problem, computation of the cross section and its Blatt-Biedenharn angular decomposition, Coulomb amplitudes, and interference. An extensive comparison with the R-matrix approach is offered. Realistic examples are used to demonstrate the techniques.

DOI: 10.1103/PhysRevC.79.044308 PACS number(s): 21.60.Cs, 24.10.Cn

I. INTRODUCTION

The problem of many-body physics on the verge of stability has a long history. Fundamental ideas date back to the works of Dirac, Wigner, Gamow, Feshbach, Rice, Fano, and others [1–10]; a number of books are available on the subject, among them are Refs. [11–15]. The problem, however, remains extremely difficult and unsettled. A multitude of new techniques attacking from different directions have emerged in recent years. The techniques based on the R-matrix reaction theory [4], which rely on the spatial separation of external and internal regions [16,17], further developed by Lane and Robson [18–21], found application in the recoil-corrected continuum shell model [22–25]. From the structure side, the shell model embedded in continuum [26–28] and the continuum shell model [29–31] are some, among many, variations of the strategies that use Hilbert space projection method suggested by Feshbach [10]. Many-body theories based on the discretized continuum along the complex momentum path have been suggested within the Gamow shell model and complex scaling methods [32–35]. From the perspective of the many-body approach all of these methods have a stationary state formalism at the core, which is extended into a complex energy plane describing decays and reactions. The broad experience with the traditional shell model, effective matrix diagonalization procedures, and even novel methods such as coupled-clusters [36] make this strategy natural. However, away from the perturbative regions of narrow noninterfering resonances these methods face significant challenges. Problems range from the physical interpretation of widths and extraction of observables to technical issues such as nonlinearity of the eigenvalue problem due to the energy-dependent effective Hamiltonian, with branches of unphysical roots in the complex plane. The solution of the complex-momentum-scattering problem, formulation of interactions in the Gamow basis, and artifacts of the projection where terms of nontrivial interaction structure emerge are among numerous obstacles.

The time-dependent approach to the continuum shell model (TDCSM) suggested here departs for the stationary state formalism in favor of reconstructing the time dependence of quantum many-body dynamics. This novel technique resolves many of the above issues. The approach reflects the time-dependent physics of unstable systems and makes the relation to observables transparent. The linearity of equations in quantum mechanics is maintained, allowing for fast numerical implementation. To demonstrate the vast power of the time-dependent continuum shell-model approach, the technique is put to test on numerous realistic examples of the present day interest and controversy. Explicit nonexponential time dependence of states is shown, and the role of self-energy terms in nuclear reaction cross sections and positions of resonances is demonstrated, suggesting that it may be responsible for the inconsistency between the traditional shell model and experimentally observed positions of unbound states. The interplay of electromagnetic transitions and particle decays is explored in the context of recent experiments and in relation to astrophysics. The strength function for dipole excitations, decays and collectivity are discussed, including questions related to the strength of the spurious center-of-mass states and their elimination. The angular momentum decomposition of the differential cross section, inclusion of Coulomb phase shifts, and large-scale applications are shown among many examples.

The time-dependent approach to the continuum shell model stems from the Feshbach projection formalism. The relevant structure and reaction features of this formalism are discussed in Sec. II. The advantage of the method lies in the transition to the time representation, which allows for the construction of the Green's function that covers the entire energy spectrum. The analogous procedure in the energy representation targets either an individual resonance or a specific energy; although commonly used, it is extremely impractical for large-scale computations. Furthermore, for narrow resonances or dense spectra the matrix inversion near the poles of the propagator becomes numerically unstable. The Gamow shell model [33,34] and complex scaling [35] are two of many methods to overcome this difficulty. The problem is not present in the

time representation. The construction of the time-dependent Green's function for the stationary, nondecaying system is discussed in Sec. III. With the Fourier transform energy representation can be obtained, where the quality of the approach is demonstrated in comparison to a direct matrix inversion and in computations of strength functions. The spectroscopic strength of the spurious center-of-mass states and methods for dealing with them are addressed in this context.

In Sec. IV the construction of the full propagator and time evolution of states in the general nonstationary situations are demonstrated. The exact solution of Dyson's equation is used to treat the decay terms, self-energy, and collectivities along the real axis. It also allows one to adjust shell-model interactions to reproduce experimental data. Realistic nuclear examples are used to show these techniques from different angles, including time dependence of survival probability, effects of decays on the strength functions and on nuclear structure, as well as the role of the self-energy terms.

The full power of the time-dependent continuum shell-model approach is demonstrated in Sec. V where the realistic nuclear applications are considered and the analysis of the related experimental data is discussed. The interplay of particle and electromagnetic channels and its astrophysical implications are shown for ^{9}C, which has been a subject of recent studies [37]. Angular decomposition of the differential cross section, Coulomb interactions, and extensive comparisons with R-matrix theory highlighting interference between resonances are examined. A large-scale example with about 10^5 resonances and hundreds of channels concludes the presentation.

II. FESHBACH FORMULATIONS

A. Structure

This section is limited to the basics of the Feshbach approach, details of which can be found in the textbooks [12,13] and in numerous publications, among them Refs. [29–31]. First, the Hilbert space is separated into bound, internal states $|1\rangle$ and an energy-labeled continuum of external states $|c;E\rangle$. The bound states are viewed as forming the traditional shell-model (SM) basis. For the continuum, $|c;E\rangle$ are observable reaction channels, with independent decay products in their eigenstates with total energy E. All intrinsic and relative quantum numbers identify the channel c. Although the treatment of the continuum-continuum interaction and many-body final-state reaction channels is possible in this framework (see Refs. [28,31]), these topics are outside the scope of the present article. The energy-continuum part of the Hilbert space can be eliminated using the projection formalism. Within the "intrinsic" SM space, also referred to as the $\mathcal{P}$ space [31], the new effective Hamiltonian $\mathcal{H}(E)$ emerges [12,13]

$$\mathcal{H}(E) = H + \Delta(E) - \frac{i}{2}W(E). \tag{1}$$

The H here is the original Hamiltonian, but its action is restricted to the intrinsic space; this implies projection operators that are omitted for the simplicity of this expression. Due to the projection, new interaction terms emerge. The Hermitian term $\Delta(E)$, commonly referred to as the self-energy, describes virtual excitations into the excluded space and the imaginary term $W(E)$ represents irreversible decays to the continuum of excluded states. These terms are expressed via energy-dependent channel vectors

$$|A^c(E)\rangle = P_{\mathcal{P}} H |c;E\rangle, \tag{2}$$

where $P_{\mathcal{P}}$ is the projection operator onto the intrinsic space. In the explicit SM basis $P_{\mathcal{P}} = \sum_1 |1\rangle\langle 1|$ and $|A^c(E)\rangle = \sum_1 A^c_1(E)|1\rangle$, where the matrix elements of the full Hamiltonian between internal and external spaces

$$A^c_1(E) = \langle 1|H|c;E\rangle, \tag{3}$$

are the energy-dependent many-body amplitudes. With the energy-based normalization of the reaction states $\langle c;E|c';E'\rangle = 2\pi\,\delta(E-E')\,\delta_{cc'}$, one obtains

$$\Delta(E) = \frac{1}{2\pi}\int\!\!\!\!\!\!- dE' \sum_c \frac{|A^c(E')\rangle\langle A^c(E')|}{E-E'} \tag{4}$$

and

$$W(E) = \sum_{c(\text{open})} |A^c(E)\rangle\langle A^c(E)|. \tag{5}$$

The bar in the notation for the integral in Eq. (4) stands for the principal value. The kinematics of the decay process is the primary source of the energy-dependence in the amplitudes, which for the channels of interest can be expressed as

$$|A^c(E)\rangle = a^c(E)\,|c\rangle. \tag{6}$$

The $a^c(E)$ is the channel amplitude and $|c\rangle$ is a constant (energy-independent) channel vector, representing the structure of the spectator components. In this work we focus on the single-particle and electromagnetic channels. The collection of equations discussing these channels, their amplitudes, kinematic behavior at low energy, and structural components, and angular-momentum recouplings are given in Appendices A and B; see also Ref. [31]. The one-body continuum part of the interaction is described by a spherically symmetric potential. Unless explicitly mentioned otherwise we assume it to be of the Woods-Saxon form with the parametrization from Ref. [38]. The one-body problem is solved numerically, in this case the width and self-energy are

$$\gamma_c(E) = |a^c(E)|^2, \quad \text{and} \quad \Delta_c(E) = \frac{1}{2\pi}\int\!\!\!\!\!\!- dE' \frac{|a^c(E')|^2}{E-E'}. \tag{7}$$

Within the traditional SM approach, in the limit of weak decays, it is common to treat the imaginary part of Eq. (1) perturbatively, assuming in the lowest order that the resonant state is described with the SM Hamiltonian eigenstate $|\alpha\rangle$, with energy and width from

$$H|\alpha\rangle = E_\alpha|\alpha\rangle, \quad \text{and} \quad \Gamma_\alpha = \langle\alpha|W(E_\alpha)|\alpha\rangle. \tag{8}$$

From Eqs. (5) and (6) it follows

$$\Gamma_\alpha = \sum_c \Gamma^c_\alpha, \quad \text{where} \quad \Gamma^c_\alpha = \gamma_c(E_\alpha)\,|\langle c|\alpha\rangle|^2, \tag{9}$$

this relates the constant channel vectors to the SM spectroscopic factors $C^2S = |\langle c|\alpha\rangle|^2$. The same overlap for an

electromagnetic decay equals to the reduced transition rate $B(\mathrm{EM}) = |\langle c|\alpha\rangle|^2$ with our normalization of amplitudes. The transition rates and spectroscopic factors are defined here as in Ref. [39]. Electromagnetic transitions are typically orders of magnitude weaker than the particle decays but the time-dependent approach allows one to treat all channels on the same footing. In the traditional SM the self-energy is usually included implicitly by fitting the parameters of the interaction to observations. However, in the above perturbation approach the correction to energy $\Delta_\alpha = \langle\alpha|\Delta(E_\alpha)|\alpha\rangle$ gives

$$\Delta_\alpha = \sum_c \Delta_c(E_\alpha)|\langle c|\alpha\rangle|^2. \tag{10}$$

From random interactions to realistic systems that range from microwave cavities to hadrons, there are numerous studies of the dynamics generated by the non-Hermitian energy-dependent Hamiltonians (1), where the complex eigenvalue problem

$$\mathcal{H}(\mathcal{E})|\alpha\rangle = \mathcal{E}|\alpha\rangle \tag{11}$$

is solved; see Refs. [27–29,40] and references therein. Summarizing the challenges, the Hamiltonian has an explicit energy dependence, making the internal dynamics highly nonlinear. The transition into a complex energy plane may be rather impractical. It causes computational complications related to the complex-plane branch cuts and unphysical roots, and the relation to observables becomes perplexing. The Hamiltonian (1) that emerges as a result of the projection contains many-body interaction terms.

B. Scattering matrix and reactions

The same dynamics can be explored with the Feshbach formalism from the reaction side, represented by the channel space. Here, the transition matrix of the scattering theory is given by

$$\mathbf{T}_{cc'}(E) = \langle A^c(E)|\left[\frac{1}{E-\mathcal{H}(E)}\right]|A^{c'}(E)\rangle, \tag{12}$$

which describes a process with an entrance channel c', an intrinsic propagation driven by the effective Hamiltonian (1), and an exit in the channel c; see Refs. [12,13]. The scattering matrix can be written as

$$\mathbf{S}_{cc'}(E) = \exp(i\xi_c)\ \{\delta_{cc'} - i\,\mathbf{T}_{cc'}(E)\}\exp(i\xi_{c'}). \tag{13}$$

The additional phase shifts $\xi_c(E)$ describe the potential scattering or a contribution of remote resonances outside of the model space. In our studies we include Coulomb phase shifts $\xi_l^C = \arg[\Gamma(1+l+i\eta)]$ that depend on the angular momentum l and the Coulomb parameter η. Then the total scattering amplitude is a sum of the nuclear terms from Eq. (12), appropriately modified by the additional phases, and the Coulomb amplitude $f^C(\theta)$; explicit equations are summarized in Appendix C. The studies reported here show no need in the additional potential contributions, although in the spirit of R-matrix techniques one can consider using hard-sphere phase shifts.

The total cross section follows directly from the above T-matrix [12]:

$$\sigma = \frac{\pi}{k'^2}\sum_{cc'}\frac{(2J+1)}{(2s'+1)(2I'+1)}|\mathbf{T}_{cc'}|^2, \tag{14}$$

where the primed variables k', s', and I' stand for the initial incident momentum, projectile spin, and target spin, respectively. The $J = J'$ is the total spin of the channel. The summation is over all incoming and outgoing channels contributing to the reaction. In the approximation of an isolated narrow resonance α of spin J_α the T-matrix in Eq. (12) is dominated by a single complex eigenvalue of the Hamiltonian $\mathcal{E}_\alpha = E_\alpha - i\Gamma_\alpha/2$. This eigenvalue is determined by treating the non-Hermitian components in the interaction perturbatively using Eqs. (8) and (9). The approximation results in the Breit-Wigner expression for cross section:

$$\sigma = \frac{\pi}{k'^2}\sum_{cc'}\frac{(2J_\alpha+1)}{(2s'+1)(2I'+1)}\,\frac{\Gamma_\alpha^c\Gamma_\alpha^{c'}}{(E-E_\alpha)^2+\Gamma_\alpha^2/4}. \tag{15}$$

An in-depth discussion, expressions for the differential cross section, and its Blatt-Biedenharn angular decomposition are presented in Appendix C; related information is also available in the literature [11,12,14,41].

III. STATIONARY SYSTEMS

A. Time evolution approach

The many-body evolution operator is at the center of the TDCSM approach. Although the method is general, we start with stationary systems. We build the evolution operator as a function of time using a Chebyshev polynomial expansion method, suggested in Refs. [42–44]. The expansion factorizes the evolution operator as follows:

$$\exp(-iHt) = \sum_{n=0}^{\infty}(-i)^n(2-\delta_{n0})J_n(t)T_n(H), \tag{16}$$

where J_n is the Bessel function of the first kind and T_n stands for the Chebyshev polynomials; see Appendix D. In comparison to the Taylor expansion or other methods of evaluating the Green's function, the Chebyshev polynomials provide a complete set of orthogonal functions covering uniformly the interval $[-1, 1]$. The asymptotic behavior of the Bessel functions assures convergence of the series (16) at long times, which allows controlling of energy resolution in the cross sections. The "angular addition" relation in Eq. (D5) provide an efficient iterative technique for evaluating Chebyshev polynomials of the Hamiltonian operator acting on any state [Eq. (E2)]. For technical details and numerical advantages, see Appendix E.

The energy representation of the retarded propagator is given by the Fourier image of the evolution operator,

$$G(E) = \frac{1}{E-H} = -i\int_0^\infty dt\ \exp(iEt)\exp(-iHt), \tag{17}$$

where H is set to have an infinitesimal negative-definite imaginary part.

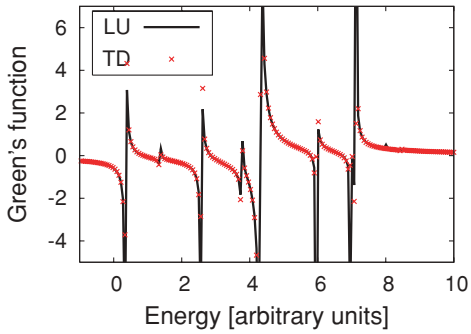

FIG. 1. (Color online) The effectiveness of the propagator expansion technique is shown using a 10-dimensional Hamiltonian matrix H selected at random. The quantity $G(E) = \Re\langle\alpha|\frac{1}{E-H+i0}|\alpha\rangle$ with an arbitrarily chosen vector $|\alpha\rangle$ is plotted as a function of E. The solid line corresponds to a numeric inversion at each energy E using the standard LU decomposition techniques [45]; the dots show the same quantity computed at 1024 points using the time-dependent Chebyshev polynomial expansion technique (marked as TD) discussed in the text.

In Fig. 1 the quality of this approach is demonstrated. Here, following Eq. (17), the Green's function in the energy representation is obtained with a direct matrix inversion for every E. This is compared to the second approach that uses a Fourier image of the evolution operator in the time representation, obtained with the Chebyshev polynomial expansion.

In the Chebyshev polynomial expansion the imaginary part of the Green's function (17) is an excellent and numerically stable representation of the δ functions associated with the energy poles in the operator. Thus, it can be used to address the strength functions and densities of states [43]. The strength function for a state $|\lambda\rangle$ is defined as

$$F_\lambda(E) = \langle\lambda|\delta(E-H)|\lambda\rangle = -\frac{1}{\pi}\,\mathrm{Im}\,\langle\lambda|G(E)|\lambda\rangle. \qquad (18)$$

It is also related to a Fourier image of the time evolution

$$F_\lambda(E) = \frac{1}{2\pi}\int_{-\infty}^{\infty} dt\, e^{iEt}\,\langle\lambda|e^{-iHt}|\lambda\rangle.$$

B. Center-of-mass separation

The translational invariance is a difficult problem for most of the many-body methods that rely on the construction of single-particle basis states that are given by the mean-field or an arbitrary confining potential. The fixed origin of the confining potential is incompatible with the translational invariance and leads to an uncertain translational momentum. The spurious center-of-mass (c.m.) states in the SM treatment appear because of the redundant coordinates. Indeed, any intrinsic SM state described in the body-fixed particle coordinates $\vec{r}_a$ is subject to a condition that it does not depend on the center-of-mass $\vec{R} = \sum_a \vec{r}_a$ that is taken as $\vec{R} = 0$. The spurious components of the Hilbert space must be removed before diagonalization; the direct construction of such many-body basis states was discussed in Ref. [46], and other projection techniques have been suggested in Ref. [47]. A more practical approach is to modify the Hamiltonian by adding a harmonically confining R^2 term that changes the translational continuum into center-of-mass oscillations [48]. The most common is the so-called Lawson method; see Ref. [49] and references therein, where intrinsic Hamiltonian is modified by adding a center-of-mass oscillator Hamiltonian

$$H_{\mathrm{c.m.}} = \frac{1}{2AM}P^2 + \frac{1}{2}AM\omega^2R^2 - \frac{3}{2}\hbar\omega$$

with some scaling β, $H(\beta) = H + \beta H_{\mathrm{c.m.}}$. Where P is the total momentum, M is the nucleon mass, and A stands for the atomic mass number. In the large β limit the physical space, associated with the $0\hbar\omega$ center-of-mass mode remains unchanged, while the other spurious states are pushed to high energy.

The time-dependent Green's function technique can be used to demonstrate the workings of the Lawson's method. As an example we consider the case of ^{20}O isotope, where the Hamiltonian is taken in the full s-p-sd-pf shell-model space with the positive-parity valence configurations restricted to the sd shell, while the negative-parity states include all possible one particle-hole excitations from the sd shell. The two-body interaction is chosen as WBP [50]. A Lawson technique is used to address the center-of-mass problem with $H_{\mathrm{c.m.}}$ included with a scaling factor that places spurious states to around 100 MeV in excitation energy. We consider a dipole operator $\vec{D} = \sum_a e_a\vec{r}_a$ where e_a is the effective charge of a particle a. In Fig. 2 the dipole strength $F_D(E)$ for excitations from the 0^+ ground state of ^{20}O is shown, i.e., the strength function Eq. (18) is plotted for a state $|D\rangle = D|0^+_{\mathrm{g.s.}}\rangle$. The choice of the magnetic projection in the operator D, a component of vector $\vec{D}$, does not matter in this case. The Chebyshev polynomial expansion of the time-dependent Green's function is used. Depending on the choice of the effective charges for the protons and neutrons, the operator $\vec{D}$ can change from the pure center-of-mass operator to the isovector operator containing no center-of-mass component. If all charges are equal $e_a = e$, then $\vec{D} = e\vec{R}$ and state $|D\rangle$ is purely a spurious isoscalar $T = 0$ center-of-mass excitation with no strength at low physical energies; see top plot in Fig. 2. An arbitrary choice of the effective charges, shown in the middle, leads to a mixed state, still containing spurious components. The physical isovector operator

$$\vec{D} = \sum_p e(\vec{r}_p - \vec{R}) = \sum_p e\left(1 - \frac{Z}{A}\right)\vec{r}_p - \sum_n e\frac{Z}{A}\vec{r}_n \qquad (19)$$

requires that $e_p = e(1 - Z/A)$ for protons and $e_n = -eZ/A$ for neutrons. As seen in Fig. 2, this choice removes the spurious center-of-mass component completely. In this work the operator $\vec{D}$ is dimensionless being expressed relative to the product of the elementary charge and the oscillator radius of the confining potential with $\hbar\omega = 1$.

Despite the apparent success, Lawson technique still has drawbacks, especially when it comes to reaction physics. Because H and $H_{\mathrm{c.m.}}$ do not commute, it is only in the limit of $\beta \to \infty$ the relative intrinsic motion is separated in the

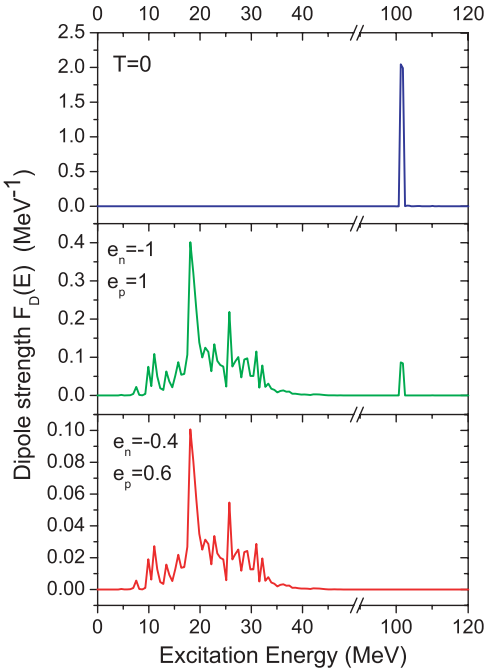

FIG. 2. (Color online) Strength function $F_D(E)$ of the dipole operator. (Upper plot) Effective charges for protons and neutrons are selected equal leading to a pure isospin $T = 0$ center-of-mass operator; only the center-of-mass states with energies around 100 MeV have nonzero strength. (Middle plot) Effective charges are selected as -1 and $+1$ for neutrons and protons, respectively, the resulting mixed operator shows strength in both center-of-mass and non-center-of-mass states. (Lower plot) The effective charges are selected as $e_n = -N/A = -0.4$ and $e_p = Z/A = 0.6$, which for ^{20}O excludes center-of-mass component from the dipole operator; the resulting strength shows no center-of-mass excitation.

diagonalization of $H(\beta)$. In practice, for the typical nuclear scales the convergence in energy for low-lying states is reached already for the values of β that place the spurious $1\hbar\omega$ center-of-mass states at about 100 MeV of excitation. Unfortunately, for such values of β the eigenstates are still contaminated by the spurious components, which may render them useless in sensitive reaction physics. The spectroscopic factors or reduced matrix elements for electromagnetic transitions, if small, can be sensitive to unphysical contaminations. On the opposite extreme, very large β effects numerical stability of any diagonalization procedure, and spurious components overshadow the physically interesting energy region. The similar problem emerges in the time-dependent method, because the widening of the spectrum leads to a deteriorating energy resolution (see Appendix D). Moreover, the potential scattering component in the cross section that comes as a collective effect from numerous tails of high-lying resonances is not expected to be cured with Lawson's technique.

In this work the center-of-mass contaminants are removed with a projection technique. The approach is exact in the Harmonic oscillator basis and very efficient as well. Indeed, all spurious center-of-mass excitations can be sequentially removed by acting $(H_{\text{c.m.}} - n\hbar\omega A)$ with $n = 1, 2 \ldots$, leaving exclusively the physical $0\hbar\omega$ center-of-mass space. The valence space places limitation on the number of center-of-mass quanta possible. For the oxygen example in Fig. 2 only $n = 1$ is possible, thus the computational overhead is small.

IV. NONSTATIONARY SYSTEMS

Next we extend the above time-dependent approach to a general nonstationary or, alternatively, energy-dependent non-Hermitian Hamiltonian (1). Although Chebyshev polynomials diverge on the complex plane, see Eq. (D6), it is possible to regularize this divergence with a complex scaling. The resulting procedure has been tested to work; however, because of complex arithmetics it is not as efficient and, more importantly, it is not as flexible as the method described below.

In this work, to obtain the propagator in the nonstationary case we take the following steps. First, we construct a stationary Green's function for the energy-independent part of the interaction, Eqs. (16) and (17), which takes most of the computational effort. Then with the exact solution to the Dyson's equation we find a full propagator that includes all other terms in the effective Hamiltonian, such as energy-dependent non-Hermitian part, self-energy, and possibly additional interaction terms needed to reproduce observations. The advantage is that once the stationary Green's function is available it takes little computational effort to modify it with different factorizable Hermitian and non-Hermitian energy-dependent corrections, thus allowing for an efficient exploration of various aspects.

If the original interaction H is perturbed by energy-dependent and generally non-Hermitian $V(E)$,

$$\mathcal{H}(E) = H + V(E) \tag{20}$$

then the relation between the original and full propagators

$$G(E) = \frac{1}{E - H} \quad \text{and} \quad \mathcal{G}(E) = \frac{1}{E - \mathcal{H}(E)} \tag{21}$$

is established through Dyson's equation $\mathcal{G}(E) = G(E) + G(E)V(E)\mathcal{G}(E)$. For the intrinsic space the perturbations from continuum occur exclusively via channel vectors, which are also referred to as the doorway states. Thus, the structure of self-energies and continuum couplings is confined to a channel subspace spanned over the energy-independent channel vectors $|a\rangle$, $|b\rangle, \ldots$

$$V(E) = \sum_{ab} |a\rangle \mathbf{V}_{ab}(E) \langle b|. \tag{22}$$

The channel subspace is a small part of the full intrinsic SM Hilbert space. We now consider all operators as matrices within the channel subspace denoting them in bold, e.g., $\mathbb{G}_{ab} = \langle a|\mathcal{G}(E)|b\rangle$ and $\mathbf{G}_{ab} = \langle a|G(E)|b\rangle$. These matrices are generally energy-dependent, here and in what follows for simplicity of notations this dependence is not shown explicitly. Then confining Dyson's equation to this subspace we find the following matrix relations:

$$\mathbb{G} = \mathbf{G}\,[\mathbf{1} - \mathbf{VG}]^{-1} = [\mathbf{1} - \mathbf{GV}]^{-1}\,\mathbf{G}, \tag{23}$$

where the matrix inversion, indicated by the $^{-1}$ superscript, takes place in the channel subspace. The scattering matrix (13)

and transition matrix (12) are confined to the same channel subspace. The T-matrix in Eq. (12) is

$$\mathbf{T} = \mathbf{a}^\dagger \mathbb{G} \mathbf{a}, \quad \text{where} \quad \mathbf{a}_{cc'} = \delta_{cc'} a^c(E) \tag{24}$$

is seen as a diagonal matrix of amplitudes for each channel $a^c(E)$. Within the eigenchannel approach [51] that we use here the perturbation due to continuum is diagonal. From Eq. (1) we have $\mathbf{V} = \mathbf{\Delta} - i\mathbf{W}/2$, where the matrix elements are

$$\mathbf{\Delta}_{cc'} = \delta_{cc'} \Delta_c(E), \quad \mathbf{W}_{cc'} = \delta_{cc'} \gamma_c(E), \tag{25}$$

with single-particle width and self-energy from Eq. (7).

In summary, the strategy for nonstationary systems is to construct in the channel space the Green's function $\mathbf{G}$ for the original part of the interaction H in Eq. (20), which is stationary and, in this work, is associated with the traditional SM Hamiltonian. Then the exact solution of the Dyson's equation (23) is used to include other terms $V(E)$ that are generally nonstationary and energy dependent. The transition matrix, cross section, or explicit time dependence of the survival probability for nonstationary states follow from the resulting nonstationary Green's function.

The following subsections demonstrate some specific applications of the procedure. If in Eq. (20) the perturbation $V(E)$ is taken to represent the energy-dependent non-Hermitian component $W(E)$, the factorized nature of such perturbation upholds unitarity, Sec. IV A, and leads to the decay of states, Sec. IV B. In addition, $V(E)$ can contain Hermitian terms that are used to modify the original Hamiltonian giving rise to collective modes, such as giant resonances, see Secs. IV C and IV D, or for the positioning of individual resonant states in accordance with experimental observations, Sec. IV E. Finally, the self-energy $\Delta(E)$ is another Hermitian component that is energy dependent and is determined by the reaction physics; its role is demonstrated in Sec. IV F.

A. Unitarity

The factorized structure $\mathbf{W} = \mathbf{a}\mathbf{a}^\dagger$, Eq. (5), implies unitarity [52,53]. Indeed, with a structure of perturbation $\mathbf{V} = \mathbf{X}\mathbf{Y}^\dagger$, where $\mathbf{X}$ and $\mathbf{Y}$ are arbitrary block matrices, another version of a geometrical series that follow from the Dyson's equation can be obtained

$$\mathbb{G} = \mathbf{G} + \mathbf{G}\mathbf{X}(\mathbf{1} - \mathbf{Y}^\dagger \mathbf{G}\mathbf{X})^{-1} \mathbf{Y}^\dagger \mathbf{G}, \tag{26}$$

which is known in computer science as Sherman-Morrison-Woodbury matrix inversion equation [45]. In Eq. (26) $\mathbf{1}$ stands for the identity matrix. Applying Eq. (26), and for a moment treating the non-Hermitian part as a perturbation $\mathbf{V} = -i\mathbf{W}/2$ with $\mathbf{X} = -i/2\,\mathbf{a}$ and $\mathbf{Y} = \mathbf{a}$, while assuming self-energy to be a part of the original H, we obtain

$$\mathbf{T} = \frac{\mathbf{K}}{\mathbf{1} + i/2\,\mathbf{K}} \quad \text{and} \quad \mathbf{S} = \frac{\mathbf{1} - i/2\,\mathbf{K}}{\mathbf{1} + i/2\,\mathbf{K}}, \tag{27}$$

where $\mathbf{K} = \mathbf{a}^\dagger \mathbf{G} \mathbf{a}$. Unitarity $\mathbf{S}\mathbf{S}^\dagger = \mathbf{S}^\dagger \mathbf{S} = \mathbf{1}$ is evident from Eq. (27), similar consideration may be found in Ref. [12].

To demonstrate the conservation of probability, in Fig. 3 we show a ^{6}He$(n,n)^6$He cross section. This fully realistic illustration is based on the p-shell valence SM space with the interactions from Refs. [54,55], the decay of states in ^{6}He is not considered. The solid line, marked as ^{6}He$(n,n)^6$He, is the full calculation with all channels included. It is well known that the cross section due to unitarity experiences discontinuities or cusps at the threshold locations where other channel(s) open [14]. Recently this was discussed in simple models [56] and within the Gamow shell-model approach [57]. In this case the elastic cross section has such a discontinuity when the inelastic channel, where ^{6}He is in its 2^+_1 final state, opens at 0.515 MeV of energy (relative to the α-particle core). The cross section for this inelastic channel is shown by the line labeled as ^{6}He$(n,n)^6$He*; it is rising sharply at the threshold taking up a portion of the flux. Because of unitarity the elastic cross section drops at the same point. To show this we plot an elastic cross section for a model calculation that includes only channels where ^{6}He is in its ground state. This is shown with a line and marked as ^{6}He$(n,n)^6$He$[0^+]$. Below the 0.515-MeV threshold the reduced model agrees with the full calculation. However, the ^{6}He$(n,n)^6$He$[0^+]$ cross section continues smoothly over the threshold because other channels are not included. The area near the threshold is magnified in the insert of Fig. 3. The difference between curves associated with the loss of flux into inelastic single-particle channel of partial wave l behaves according to the phase-space volume as $\Theta(\epsilon)\,\epsilon^{l+1/2}$, where ϵ is the energy above the threshold and $\Theta(\epsilon)$ is the Heaviside step function, see Refs. [14,41] and Appendix A. Thus, in this example the discontinuity could be visible only in the derivative. Another phenomenon to note, is that the second $3/2^-$ resonance does not appear in the full calculation, because it is broad due to inelastic decay channels. These channels are not included in the truncated model, allowing for the resonant peak to become visible.

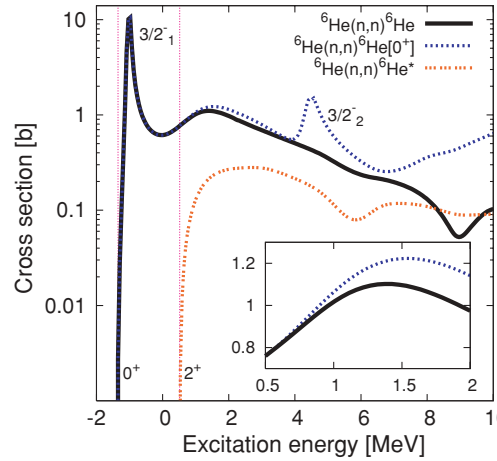

FIG. 3. (Color online) Cross section for the neutron scattering ^{6}He(n,n). The solid curve is the total elastic cross section ^{6}He$_{\text{g.s.}}(n,n)^6$He$_{\text{g.s.}}$. For the dotted line, labeled as ^{6}He$(n,n)^6$He$[0^+]$, only channels with ^{6}He in its 0^+_1 ground state are considered. The dotted curve marked as ^{6}He$(n,n)^6$He* shows the inelastic cross section with ^{6}He in the 2^+_1 final state. The lowest thresholds for the channels 0^+_1 and 2^+_1 are marked with the vertical grid lines, and the two $3/2^-$ resonances in ^{7}He are labeled. Energies are relative to the α-particle core. The insert in the lower right uses linear scale and magnifies the area near the 2^+_1 threshold.

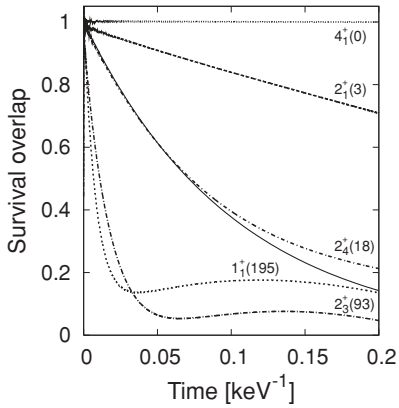

FIG. 4. Time evolution of several low-lying states in ^{24}O. The absolute value of the survival overlap $|\langle\alpha|\mathcal{U}(t)|\alpha\rangle|$ is shown as a function of time. Different lines, as marked, correspond to states $\alpha(E_\alpha, \Gamma_\alpha)$: $2_1^+(4.180, 2.7)$, $1_1^+(5291, 195.1)$, $4_1^+(6947, 0.0)$, $2_3^+(8107, 92.5)$, and $2_4^+(9673, 17.5)$. They are eigenstates of the traditional USD SM but are nonstationary resonances in the TDCSM, except for the 4_1^+ which due to its high spin does not decay within the *sd* valence space. To emphasize the nonexponentiality in the decay law the unmarked solid line shows the $\exp(-\Gamma_\alpha t/2)$ function with parameters for the 2_4^+ state.

B. Time evolution of decaying states

Next the explicit time evolution of nonstationary states is discussed with the help of the above Green's function. We use the inverse Fourier transform to define an evolution operator for the restricted $\mathcal{P}$ space

$$\mathcal{U}(t) = -\frac{1}{2\pi i}\int_{-\infty}^{\infty} \mathcal{G}(E)\, \exp(-iEt)\, dE. \qquad (28)$$

In Fig. 4 the time evolution of the overlap $|\langle\alpha|\mathcal{U}(t)|\alpha\rangle|$ for several states α in ^{24}O is shown. For this study, the channel space is extended to include the states of interest $|\alpha\rangle$, so that the corresponding expectation values of the Green's function are available. This can be done with the general approach. However, it is most interesting to discuss how the eigenstates of the original stationary SM Hamiltonian H are perturbed by the presence of the continuum. In that case if $H|\alpha\rangle = E_\alpha|\alpha\rangle$, no additional numerical work is needed because for any state $|c\rangle$, $\langle\alpha|G(E)|c\rangle = \langle\alpha|c\rangle/(E - E_\alpha + i0)$.

In Fig. 4 the states $|\alpha\rangle$ are the eigenstates of the traditional USD SM Hamiltonian [58]; however, depending on the quantum numbers and open channels they are not in general stationary within the TDCSM. When the non-Hermitian components are small such states can be viewed as resonances. If the effective Hamiltonian is energy independent, which is the case for a stationary system or in the Breit-Wigner description of isolated narrow resonances, then $\mathcal{U}(t) = \exp(-i\mathcal{H}t)$. For this example we assume the self-energy term to be a part of the USD interaction. See Sec. IV F for an all-inclusive treatment. We select several most representative in terms of the decay width states: $2_1^+(4.180, 2.7)$, $1_1^+(5291, 195.1)$, $4_1^+(6947, 0.0)$, $2_3^+(8107, 92.5)$, and $2_4^+(9673, 17.5)$, which are listed here with their excitation energy followed by the decay width, both in keV. These parameters are quoted from the traditional SM using definitions in Eq. (8). The overlap $|\langle\alpha|\mathcal{U}(t)|\alpha\rangle| = 1$ for the stationary states, such as 4_1^+, which cannot decay in this model due to high angular momentum. In accord with the Breit-Wigner approximation, the decay of narrow isolated resonances is well described with the exponential law $|\langle\alpha|\exp(-i\mathcal{E}_\alpha t)|\alpha\rangle| = \exp(-\Gamma_\alpha t/2)$, which at small times, is close to linear $|\langle\alpha|\exp(-i\mathcal{E}_\alpha t)|\alpha\rangle| \approx 1 - \Gamma_\alpha t/2$. The broad resonances exhibit nonexponential decay law; this behavior is expressly visible in the time evolution of the 1_1^+ and 2_3^+ states. The nonexponential decay of open quantum systems is an extensively discussed topic, with issues ranging from specific applications, experimental observations and quantum tunneling to Zeno paradox and theory of measurement, see Refs. [29,59,60] for example.

C. Collectivity and strength function

While the non-Hermitian components in the Hamiltonian discussed above spur irreversible decays the Hermitian terms of factorizable nature are known to be responsible for the collective phenomena such as giant resonances. Figure 5 demonstrates the emergence of dipole collectivity in ^{22}O. This choice of the nucleus is motivated by the recent interest in the distribution of the dipole strength in neutron-rich oxygen isotopes [61]. Here, the same WBP model Hamiltonian

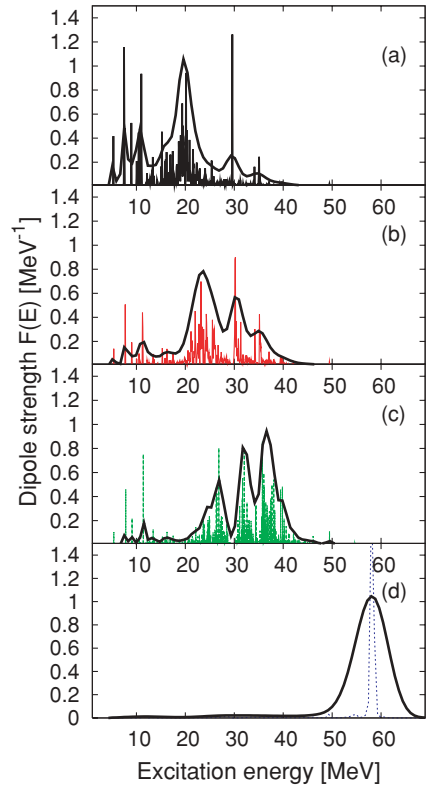

FIG. 5. (Color online) Strength function $F_D(E)$ of the isovector dipole operator in ^{22}O. Panel (a) shows the strength function of the original SM Hamiltonian, for panels (b), (c), and (d) the additional dipole collectivity is introduced into the Hamiltonian with strength $\kappa = 10$, 20, and 60 MeV, respectively. All figures include the smoothed curve that profiles the behavior of the strength distribution.

is used for ^{22}O as in Fig. 2. The spurious center-of-mass states are removed with the projection, and the collective dipole strength is added to the SM Hamiltonian by including energy-independent $V = \kappa|D\rangle\langle D|$ in Eq. (23). As before, $|D\rangle = D|0^+_{\text{g.s.}}\rangle$ and D is the isovector dipole operator (19). The dependence of the dipole strength $F_D(E)$ on the parameter κ is demonstrated. As κ is increasing from Figs. 5(a)–5(d) the enhanced dipole collectivity in the Hamiltonian gives rise to a pronounced giant dipole resonance. Finally, in Fig. 5(d), the entire dipole strength is concentrated in a single state.

D. Collectivity and decay

Targeting the question of interplay between the dipole collectivity and particle decay we further extend our example of ^{22}O. In addition to the dipole collectivity we allow for the neutron decay from the $1p0f$ shell by adding the corresponding energy-dependent non-Hermitian terms. We generalize Eq. (18) for the states λ embedded in continuum

$$F_\lambda(E) = -\frac{1}{\pi}\,\text{Im}\,\langle\lambda|\mathcal{G}(E)|\lambda\rangle. \tag{29}$$

In the limit of bound states this equation coincides with Eq. (18). Within the projection approach, however, there are subtle complications. In the intrinsic space the effective Hamiltonian is energy dependent, and the full set of eigenvectors for this nonlinear problem in Eq. (11) is generally not complete within the $\mathcal{P}$ space. Thus, the normalization condition

$$\int_{-\infty}^{\infty} F_\lambda(E)dE = \langle\lambda|\lambda\rangle \tag{30}$$

holds true only for the energy-independent, although not necessarily Hermitian, effective Hamiltonian. Nevertheless, the definition (29) is good, practical, and appropriate for examining the strength distribution in a way that is continuous in going from bound states to resonances. This minor mathematical complication is common when a continuum of states is portrayed with a set of discrete resonances. As demonstrated in what follows, the deviation in Eq. (30), and thus the lack of completeness, are small.

In Fig. 7 we show the isovector dipole strength $F_D(E)$ built on the ^{22}O ground state in the presence of $l = 1$ neutron decay from the states with excitations in $0f1p$ shell. As before, the WBP SM interaction is used, limited to all sd-valence configurations and $1\hbar\omega$ excitations into the lower p and upper fp oscillator shells. The original SM interactions seem to lack the dipole collectivity, thus the collectivity was induced with an additional factorizable dipole-dipole interaction with $\kappa = 20$ MeV strength. To be more specific, the distribution of the dipole strength in Fig. 5(c) was judged to be realistic, and the corresponding Hamiltonian is selected for the discussion below. To better explore the effects of the continuum besides the non-Hermitian part that comes from the reaction calculations in the Woods-Saxon potential, we also consider cases where $W(E)$ is scaled by factors of 3 and 10, referred to as medium and strong coupling limits in the following discussion.

With the oscillator wave functions with $\hbar\omega = 1$ the total SM dipole strength is known analytically to be $\langle D|D\rangle = \frac{3}{4\pi}\frac{28}{11} \approx 0.6076$. This quantity is 0.6072 when reproduced by the integrated strength in Eq. (30), obtained from the time-dependent Green's function technique. This shows an excellent numerical quality of both the time-dependent Green's function approach and the inclusion of real-valued corrections via the solution of Dyson's equation. As already discussed, the energy dependence of the Hamiltonian modifies the cumulative value of the dipole strength. With realistic decay the integrated strength is 0.5849; for medium and high continuum couplings the strength is 0.5639 and 0.5666, respectively.

Being embedded in continuum, the peaks associated with individual resonances become broader and shorter, while the averaged distribution of the strength shown by the solid line in Fig. 6, is not affected significantly by the decays. For an in-depth picture, the low-lying energy region is shown in Fig. 7. Curve (a) in Fig. 7 corresponds to the calculation with realistic coupling to continuum; decay widths at these low energies are small and indistinguishable from the traditional shell-model results. Curves (b) and (c) in Fig. 7 show the medium and strong couplings to the continuum, when all

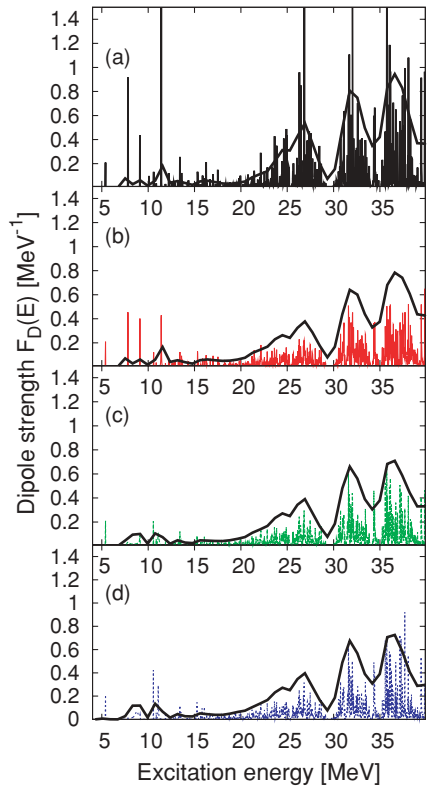

FIG. 6. (Color online) Isovector dipole strength function $F_D(E)$ for ^{22}O. The panel correspond to (a) no decay, (b) realistic decay width computed with Woods-Saxon potential [38], (c) enhanced by a factor of 3 coupling to continuum, and (d) a factor of 10 stronger decay than realistic. For this calculation the dipole collectivity is induced with $\kappa = 20$. The dipole operator is computed with Harmonic oscillator wave functions with $\hbar\omega = 1$ and is expressed here in the corresponding units. The solid line in each case represents a smoothed curve showing the general trend.

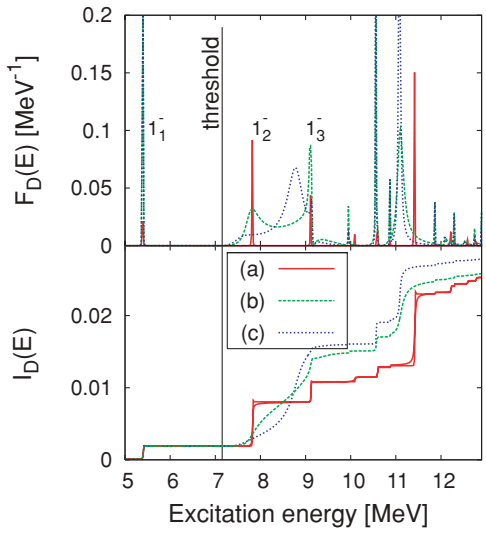

FIG. 7. (Color online) Isovector dipole strength function for ^{22}O. Top panels depicts the strength function $F_D(E)$ and the lower panel shows the cumulative strength up to a given energy $I_D(E)$ (integral of the curves on the upper panel). The curves correspond to (a) realistic decay width computed with Woods-Saxon potential [38]; (b) enhanced by a factor of three coupling to continuum; (c) a factor of 10 stronger decay than realistic. The standard SM result is almost indistinguishable from the curve (a), on the lower figure it may be noticed by its characteristic sharp steps. The model is the same as in Fig. 6.

widths are artificially enhanced by factors of 3 and 10, respectively. In the upper panel of Fig. 7 the strength function is shown as a function of energy, as in Fig. 6 but on a different scale. Note that curve (a) in Fig. 7, which is a set of δ functions, is scaled on the upper panel and hence only relative heights of peaks can be discussed. As the coupling to continuum is artificially increased the effects of interaction between 1^-_2 and 1^-_3 resonances are visible. This is known as energy attraction and width repulsion, see Refs. [40,62]. The lowest three 1^- states are marked in Fig. 7, only the neutron-bound one 1^-_1 at 5.313 MeV in this model may have been experimentally observed at about 5.8 MeV of excitation.

The lower panel in Fig. 7 represents an integrated strength

$$I_\lambda(E) = \int_{-\infty}^{E} F_\lambda(E')dE', \tag{31}$$

i.e., the area under the strength function curve up to a certain energy. The lines for the traditional discrete-level SM and for the realistic decay are almost indistinguishable. Note, that for the traditional SM the integrated strength is a sum of the reduced transition rates

$$I_D(E) = \sum_{\alpha}^{E_\alpha < E} B(E1;\alpha \to 0^+_{\text{g.s.}}); \tag{32}$$

the curve has a steplike behavior with steps at every contributing SM eigenvalue E_α. For medium and strong couplings to the continuum the strength distribution transforms into a smooth curve. In the strong decay limit there is an accumulation of dipole strength in the low end of the spectrum. Although the decay strength here is not realistic, this shows the interplay of the dipole collectivity and collectivization by the decay, see Refs. [63,64].

E. Position of resonances

The reaction kinematics is very sensitive to the energy, see Appendix A, which may deem the SM energies useless in calculations of reaction cross sections and lifetimes. Thus, it is a common practice to combine the spectroscopic factors and the reduced transition rates from the traditional SM with the experimentally observed Q values. This practice can be extended in the TDCSM. Although the discrepancies in energies of states can have different sources, varying from poorly selected interaction or small valence space to self-energy terms, here we demonstrate how interaction can be fitted to position resonances according to observation. Similar fitting is typical in experimental analyses with the R-matrix approach.

Positioning of the resonances in TDCSM approach is achieved by adding a Hermitian correction term V in the factorizable form $V = \sum_\alpha |\alpha\rangle V_\alpha \langle\alpha|$, where V_α are interaction parameters to be adjusted and α's are the stationary SM states, $H|\alpha\rangle = E_\alpha|\alpha\rangle$. In the TDCSM each such state becomes a resonance, whose position on the real axis of energy is then shifted approximately to $E_\alpha + V_\alpha$.

An example of such a shift is demonstrated in Fig. 8, where the cross section for the elastic $^{23}\text{O}(n,n)^{23}\text{O}$ reaction is shown. A model same as the one in Fig. 4 is used. The solid line depicts a cross section based on the USD shell-model Hamiltonian, while the dashed line shows a single state 1^+, originally at 5.29 MeV of excitation, shifted upward by exactly $V_{1^+} =$ 1 MeV. The new resonance peak, being at a higher energy, is broader and a contribution from its tail is visible at higher energies, whereas all other resonances and features in the cross section remain the same. The minimal computational overhead, and thus ability to try multiple adjustments, is an advantage of the TDCSM.

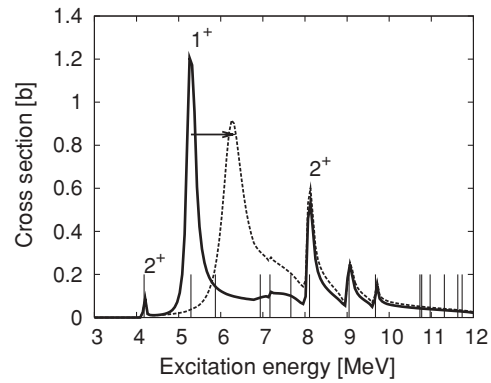

FIG. 8. The total $l = 2$ cross section of $^{23}\text{O}(n,n)^{23}\text{O}$ reaction depicting resonances in ^{24}O is shown for the original USD interaction (solid line) and for the Hamiltonian with the location of the first 1^+ state shifted by 1 MeV (dashed line). The shift of this state from 5.29 to 6.29 MeV in the excitation energy is indicated with an arrow. Additional x-axis tick marks show locations of the USD SM levels.

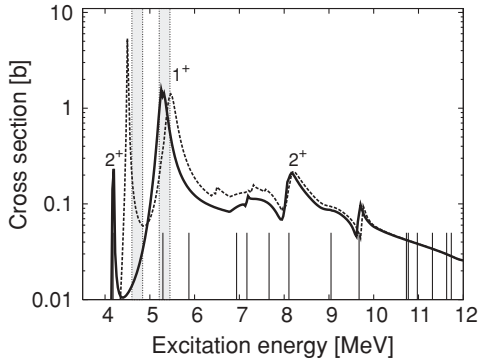

FIG. 9. The total $l = 2$ cross section of ^{23}O$(n, n)^{23}$O reaction, the solid line and tick marks are identical to those in Fig. 8. The dashed line shows the cross section computed with energy-dependent self-energy terms included. The shaded areas show experimental values from Ref. [66] with uncertainties, $E_{2_1^+} = 4.72(11)$ MeV and $E_{1_1^+} = 5.33(12)$ MeV.

F. Self-energy

The role of self-energy terms in the same model of ^{24}O via ^{23}O$(n, n)^{23}$O reaction is shown in Fig. 9. These terms emerge from the virtual excitations into the continuum of scattering states. In the channel space, which now covers all open and closed channels the Hermitian self-energy part is diagonal, see Eq. (25). The terms $\Delta_c(E)$ in Eq. (7) can be computed numerically for every channel of interest. The behavior being dominated by the phase-space integral is discontinuous near thresholds, see Appendix A. This is consistent with the discontinuity of the spectroscopic factors, recently addressed in Refs. [57,65]. In this study, the near threshold behavior is assumed by virtue of Eq. (A2). It is analogous to the energy dependence of the width in potential scattering that is well described with the $\gamma_c(\epsilon) \sim \epsilon^{l+1/2}$ scaling, typically up to several MeV above the threshold [39], where ϵ is the energy relative to the threshold. The number of virtual channels is limited, but the results presented here are stable with respect to the truncation in the channel space. Virtual transitions to continuum via high-lying states are suppressed by the energy denominator and the complex many-body structure of those states, where the spectroscopic overlap is very small. The effect is analogous to the compound resonances, which are narrow due to complexity in the structure, despite high excitation energy. In Fig. 9 the $l = 2$ cross section is shown with and without the self-energy term $\Delta(E)$.

The positions of the low-lying 2^+ and 1^+ resonances shift upward due to the virtual interaction with continuum. Although this example is intended to demonstrate the effect of self-energy, it is remarkable that the resulting model is in good agreement with experiment and partially corrects the discrepancy in the traditional USD shell model. In Fig. 10 the predictions for the 1^+ and 2^+ resonances in ^{24}O from various theoretical calculations are summarized and compared to the recent experimental data [66]. It appears that the older USD interaction that was fitted to bound states is improved substantially after the inclusion of continuum effects. This matter requires further systematic investigation.

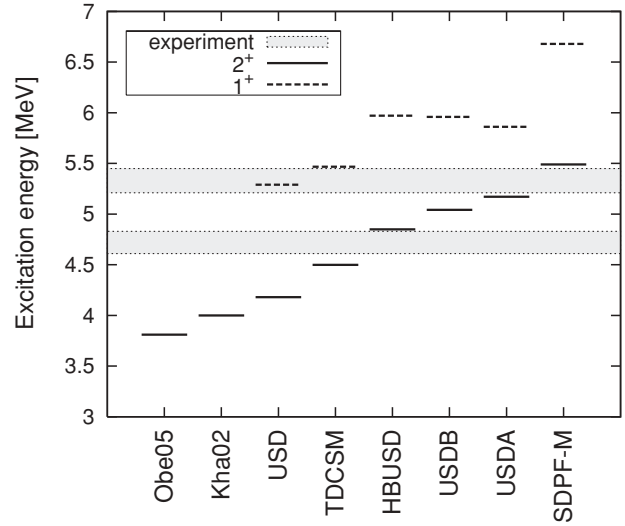

FIG. 10. The predicted energies $E_{2_1^+}$ and $E_{1_1^+}$ of the 2_1^+ (solid line) and 1_1^+ (dashed line) excited states from different theoretical calculations are compared with experiment. The experimental values of $E_{2_1^+} = 4.72(11)$ MeV and $E_{1_1^+} = 5.33(12)$ MeV are from Ref. [66], with uncertainties as indicated by the shaded areas. The theoretical studies labeled as USD [67], USDA and USDB Ref. [68], Obe05 [69], Kha02 [70], HBUSD [30,58], SDPF-M [71] can be found in the corresponding references.

V. APPLICATIONS

A. Resonance spectroscopy of ^{9}C

In a recent experiment [37] the structure of ^{9}C was studied using the elastic scattering of ^{8}B on protons. As a result of the R-matrix analysis a new excited state in ^{9}C was found at an excitation energy of 3.6 MeV and its spin and parity are determined as $5/2^-$. These findings are supported by the TDCSM, which describes the observed cross section and positions of resonances relatively well. The conclusions in Ref. [37] depend on the proper evaluation of the cross section for the contaminating inelastic reaction ^{8}B$(2^+_{\text{g.s.}})(p, p')^8B(1_1^+)$. The evaluation of this cross section with TDCSM and with other methods is discussed in Fig. 11. The TDCSM study is based on the WBP [50] interaction with continuum described by the Woods-Saxon potential, as parametrized in Ref. [38]. The bulk of the contribution to the cross section comes from the $3/2_2^-$ resonance, which interferes with a higher-lying broad $3/2_3^-$ state. The total cross section and the one for $J = 3/2^-$ channels exclusively are shown for comparison. The Breit-Wigner description, Eq. (15), for which the reduced widths are calculated with the spectroscopic factors of the traditional SM, is shown for both the $3/2^-$ states. The problem with the energy-independent width in the Breit-Wigner picture precludes a correct near-threshold behavior. The interference between the resonances is a primary source of the discrepancy between the TDCSM and R-matrix approach, the latter including a single $3/2^-$ resonance. An in-depth comparison of R-matrix and TDCSM is presented in another example in Sec. V B.

It is compelling to discuss the astrophysical implications from the newly observed $5/2^-$ resonance for the

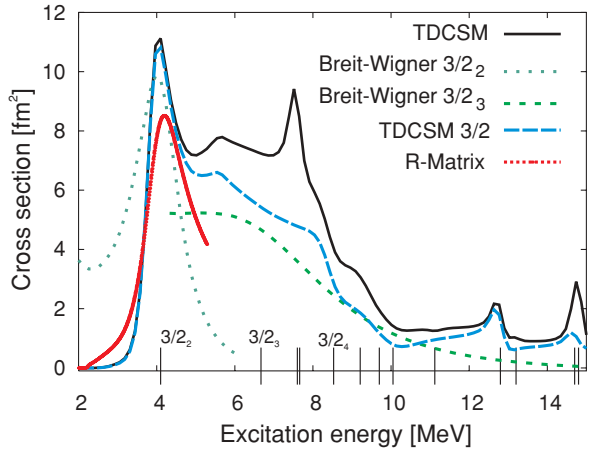

FIG. 11. (Color online) The inelastic cross section for the scattering process $^8\mathrm{B}(2^+_{\mathrm{g.s.}})(p,p')^8\mathrm{B}(1^+_1)$. The solid curve corresponds to a full TDCSM calculation with all $l=1$ channels with spin and parities $1/2^-$, $3/2^-$, and $5/2^-$. The blue dotted curve shows the TDCSM cross section when only $J^\pi = 3/2^-$ channels are included in the model. The red dashed curve is a result of the R-matrix calculation from Ref. [37] that uses similar reaction parameters and takes into account only the $3/2^-_2$ resonant state. The figure contains two Breit-Wigner curves, Eq. (15), for the $3/2^-_2$ and $3/2^-_3$ states. The locations of resonant states in ^{9}C are marked with the vertical tick marks.

$^8\mathrm{B}(2^+_{\mathrm{g.s.}})(p,\gamma)^9\mathrm{C}(3/2^-_{\mathrm{g.s.}})$ process. The electromagnetic transition is a theoretical component in this investigation with no direct experimental data available. Because electromagnetic transitions are typically much weaker than the particle decays, the perturbative treatments based on the spectroscopic factors and Breit-Wigner expressions for the widths are often used. The perturbative approach in the photon channels with the SM embedded in continuum for (p,γ) reactions was demonstrated in Ref. [26]. In the TDCSM the γ channels are regarded on the same footing with the particle channels, because the time-dependent approach permits a reliable treatment of resonances that differ in the width by many orders of the magnitude. The cross section for the (p,γ) reaction populating the ground state of ^{9}C is shown in Fig. 12. The upper panel, on a large energy scale, depicts several resonances from the TDCSM calculation. The $1/2^-_1$ state has been known before and the question here centers on the role of a newly discovered $5/2^-_1$ state.

From the standpoint of the traditional SM, the spectroscopic factors for the $5/2^-_1$ state are $C^2S(p_{3/2}) = 0.11$ and $C^2S(p_{1/2}) = 0.68$, which lead to the total proton decay width of $\Gamma^p_{5/2^-_1} = 1.44$ MeV, see Eqs. (8) and (9). For the electromagnetic decay $B(M1) = 0.075\mu_N$ and $B(E2) = 2.6\ e^2\ \mathrm{fm}^4$, the corresponding partial decay widths are $\Gamma^{M1}_{5/2} = 40$ meV and $\Gamma^{E2}_{5/2} = 1.3$ meV.

The (p,γ) reaction in the astrophysically relevant region of energies is presented in the lower panel of Fig. 12. Here the TDCSM is used to assess the importance of the $5/2^-$ resonance, and hence the contributions to the cross section from different angular momenta of the channels are separated. The resonance $1/2^-$ is dominating, while the $5/2^-$ peak is

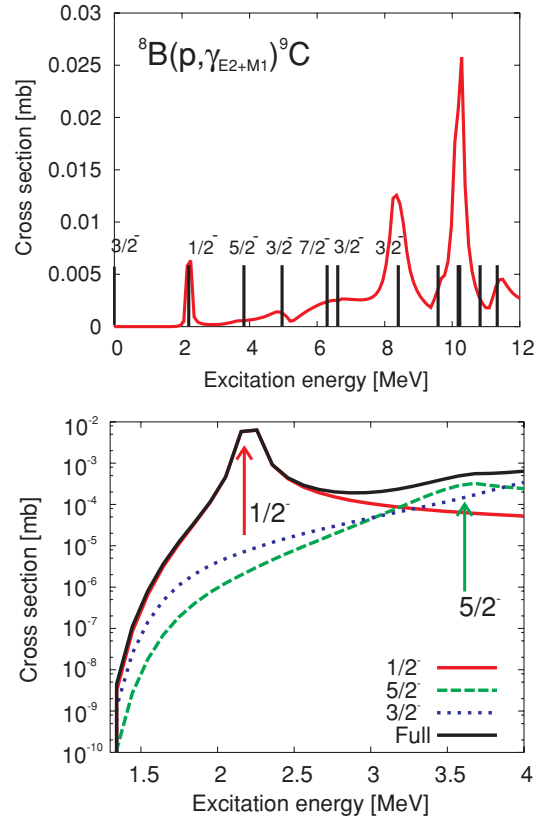

FIG. 12. (Color online) The astrophysically interesting proton capture cross section for the $^8\mathrm{B}(2^+_{\mathrm{g.s.}})(p,\gamma)^9\mathrm{C}(3/2^-_{\mathrm{g.s.}})$ reaction. All $l=1$ proton partial wave channels are included as well as all $M1$ and $E2$ electromagnetic channels. The PWT interaction with adjusted to the Q values from $^8\mathrm{B}(p,p)^8\mathrm{B}$ experiment [37]. Upper panel shows a general overview of the cross section, while the lower panel magnifies the low-energy region. Contributions from the most important angular-momentum channels are separated. Arrows indicate the locations of the $1/2^-_1$ and newly observed $5/2^-_1$ resonances.

weak with negligible contribution at low energy. From this we conclude that the contribution of the $5/2^-$ resonance to the astrophysical (p,γ) process is unimportant.

B. The ^{7}Be(p,p') reaction

In this subsection we demonstrate the TDCSM in the $^7\mathrm{Be}(p,p')$ study. This discussion aims at the resonances in the ^{8}B system that are of interest in astrophysics. The possibility of several, yet unobserved, low-lying states found in some of the traditional SM studies [72] and suggested by Halderson using the recoil-corrected continuum shell model [22,24] is important, and experimental efforts to find them are underway [73,74]. As it was discussed by Halderson [22,24] the observation of such states and interpretation of the cross sections demands a theory that combines structural many-body physics with an advanced treatment of reactions. States predicted with the traditional SM approach may not be visible in reaction studies due to the complex nature of the interference between overlapping resonances. On the other

hand the R-matrix approach lacks the structural information and requires too many parameters; high sensitivity to these parameters and their phases may prevent a definite conclusion. The study below shows the success of the TDCSM in confronting these features; the presentation is done in parallel with the R-matrix treatment to affirm the consistency of the new theory.

For this study we use a Hamiltonian that consists of the SM interaction WBP [50] and interaction with one-body continuum given by the Woods-Saxon potential, with parameters from Ref. [38]. The Hamiltonian describes the energies of the experimentally observed $2^+_{\text{g.s.}}$, 1^+_1(0.7695 MeV), and 3^+_1(2.32 MeV) states relatively well. We adjust the reaction Q values relative to a narrow 1^+_1 resonance via modification of the channel thresholds so that the experimentally observed proton separation energy and excitation energy of the first excited $1/2^-$ (0.4291 MeV) state in ^{7}Be are reproduced. The quality of the WBP Hamiltonian does not warrant inclusion of self-energy neither any separate adjustment of the observed broad 3^+_1 state. However, unlike most SM interactions, the WBP predicts nearly degenerate low-lying 1^+_2 and 0^+_1 states at 1.94 and 1.97 MeV in the excitation energy. The objective is to see if and how these states can be detected experimentally. The TDCSM calculation presented here includes a Blatt-Biedenharn angular decomposition [75] and Coulomb effects, see Appendix C. The elastic ^{7}Be$(p, p)^7$Be cross section is shown in Figs. 13 and 14(a).

The R-matrix studies [4], depicted in Figs. 13 and 14(b), are conducted in parallel and include five $l = 1$ resonances, namely 1^+_1, 1^+_2, 0^+_1, 3^+_1, and 2^+_2. The channel radii for the ^{7}Be$_{\text{g.s.}}$ and the first excited state are selected at 4.5 fm. The locations of the resonances are adjusted to reproduce exactly the TDCSM results via boundary conditions, see arguments in Ref. [76]. Traditional SM calculation is used for all R-matrix decay amplitudes, see Table I.

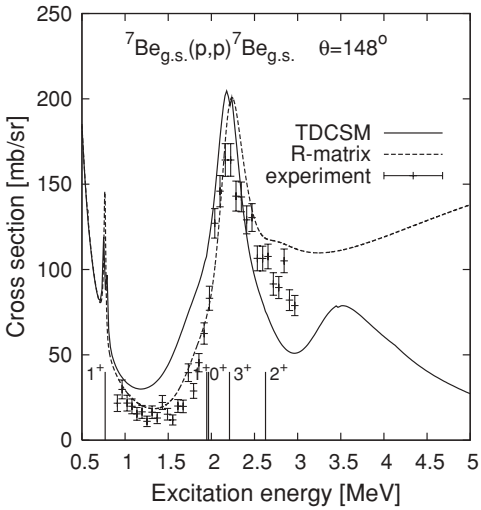

FIG. 13. Elastic ^{7}Be$(p, p)^7$Be differential cross sections at 148° from TDCSM (solid line) and from R-matrix study (dashed line) are shown. Experimental data are from Ref. [74], the experimental error bars do not include a 12° uncertainty in the angle.

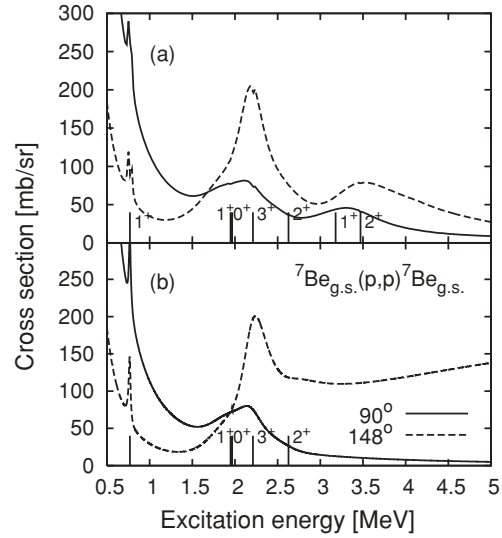

FIG. 14. Elastic ^{7}Be$(p, p)^7$Be differential cross section from TDCSM (a) and from R-matrix study (b). In both cases the solid line corresponds to 90° scattering angle and the dashed line to 148°. The tick marks indicate location of resonances and their spin parity. For the R-matrix study (b) only included resonances are marked.

The experimental data from Ref. [74] and theoretical predictions from the TDCSM and R-matrix are shown in Fig. 13. Despite a relatively good overall agreement the reader is urged not to make a detailed comparison with experiment, both theoretical models use resonances predicted by the WBP SM interaction. This interaction was selected to contemplate the suggestion about the low-lying 1^+_2 and 0^+_1 resonances suggested in Ref. [22], for which no evidence was found in Ref. [74]. Here we concentrate on the theoretical models. Figures 14–16 and Fig. 18 all have the TDCSM results in the upper panel and R-matrix results in the lower panel, for the purposes of comparison. There is an overall consistency. However, there are a few apparent differences summarized below:

(i) Only a finite number of resonances can be technically included and successfully fitted with the R-matrix method. Here we include all states up to 3 MeV of excitation energy, they are indicated with the tick marks.

TABLE I. R-matrix amplitude parameters in the j-coupling scheme. The amplitudes here are overlaps $\langle\alpha|c\rangle$ between the channel vectors c and SM eigenstates α. The channels for $l = 1$ proton in the continuum and ^{7}Be in the ground state and first excited state are listed in columns. The eigenstates α of ^{8}B are in rows, the spin, parity, and excitation energy are indicated.

J^π	E(MeV)	$p_{3/2}$(g.s.)	$p_{1/2}$(g.s.)	$p_{3/2}$	$p_{1/2}$
1^+_1	0.7693	−40.563	0.303	0.867	−0.138
1^+_2	1.947	0.597	0.826	0.284	0.240
0^+_1	1.967	0.693	0	0	−0.918
3^+_1	2.2098	0.612	0	0	0
2^+_2	2.628	0.149	0.326	−0.632	0

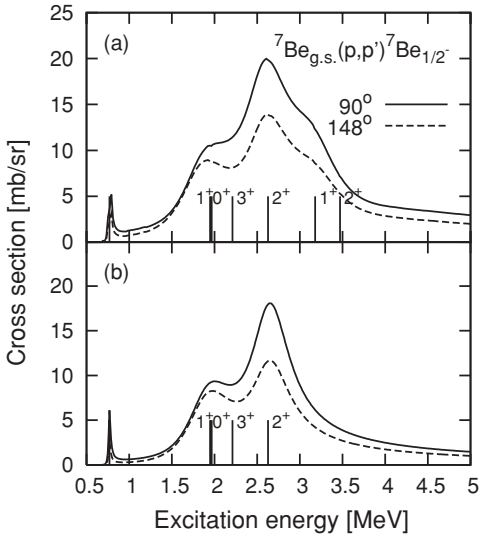

FIG. 15. Inelastic $^7\mathrm{Be}_{\mathrm{g.s.}}(p, p')^7\mathrm{Be}_{1/2^-}$ differential cross sections at 90° (solid line) and at 148° (dashed line) are shown from TDCSM approach (a) and from the R-matrix study (b). Tick marks and line styles are identical to those in Fig. 14.

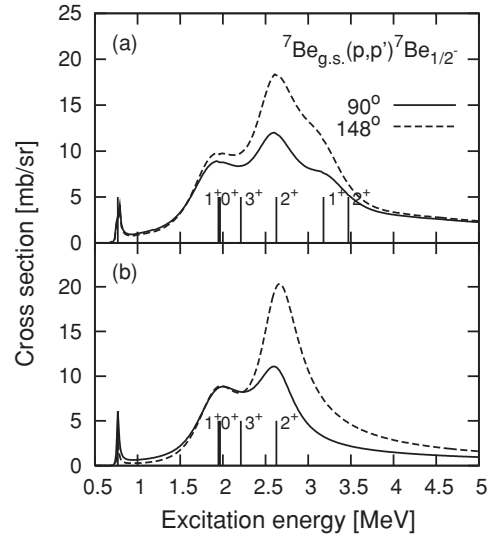

FIG. 16. Inelastic $^7\mathrm{Be}_{\mathrm{g.s.}}(p, p')^7\mathrm{Be}_{1/2^-}$ cross section where the phase of $J^\pi = 2^+$ channel corresponding to a single-particle with $j = 1/2$ in the continuum and ^{7}Be in its ground state has been reversed. The figure is not expected to represent a realistic situation but is to be compared with Fig. 15 that has identical notations and markings.

This leaves out the third 2_3^+, and the peak associated with it does not appear in the cross section. Furthermore, with this truncation the interference between the 2^+ resonances is lost, while it is present in the TDCSM.

(ii) The R-matrix is constructed using amplitudes and energies of the states from the traditional SM, Table I. A better approach would be to use the TDCSM and match the poles in the scattering matrix.

(iii) The R-matrix, in its traditional construction, includes an additional hard-sphere phase shifts. Note the increase in the elastic $\theta = 148^\circ$ cross section at higher energy, Figs. 13 and 14(b). This behavior mimics the contribution from all remote resonances. Despite truncation of the valence space the continuum shell model has a lot of high-energy resonances included and there is no need in the additional phase shifts. Similar to the Coulomb interaction, introduction of the additional phase shifts presents no technical difficulty. The reaction contributions coming from outside the SM valence space is an important topic but is to be discussed elsewhere.

Although both the theoretical approaches are in good agreement with observation [74], Fig. 14 shows that the contribution from the states $1_2^+, 0_1^+$, and 2_2^+ is too small to be detected in the elastic scattering. Thus, an inelastic process $^7\mathrm{Be}_{\mathrm{g.s.}}(p, p')^7\mathrm{Be}_{1/2^-}$ has been suggested [22,24]. The results for inelastic scattering from TDCSM, Fig. 14(a), and from R-matrix are shown in Fig. 15(b). The cross section is now dominated by the 2_2^+ resonance with a visible peak due to 1_2^+ and 0_1^+ states.

The angular dependence of the differential cross section allows one to obtain some structural information about the states, this information is more stringent than the typical comparison of excitation energies and spectroscopic factors. The 2_2^+ resonance is a good example of this because it has a significant anisotropy, which depends on its structure. For this reaction, with $l = 1$ scattering partial wave, Eq. (C6) has the form $\frac{d\sigma}{d\Omega} = \frac{1}{8k^2}[B_0 + B_2 P_2(\cos\theta)]$ and the sign of B_2 depends on the relative phases. This effect is demonstrated in Fig. 16, where the sign in the phase of the $J^\pi = 2^+$ channel corresponding to the single particle with $j = 1/2$ coupled to the ^{7}Be ground state has been changed to the opposite. In the R-matrix approach it is a trivial change in the sign of the corresponding amplitude, while in TDCSM approach all phases are fixed by the many-body structure and to obtain Fig. 16(a) an extra sign had to be introduced in the code making it erroneous. The comparison between Figs. 15 and 16 shows that, although the 2_2^+ resonance is at an identical energy with identical spectroscopic factors and partial decay widths, the anisotropy of the cross section is quite different. As predicted by the TDCSM based on the WBP interaction the cross section for the 2_2^+ resonance should be higher at a scattering angle of $\theta = 90^\circ$. This and similar predictions can be helpful in experimental identification of resonances.

Next we direct our attention to the two states 1_2^+ and 0_1^+. In this model, due to a choice of the WBP intrinsic interaction, these states appear low in energy, but their positions are debated. Most shell-model studies predict them to be much higher, and they have not been observed experimentally [74]. Moreover, how they could be observed is another question. Thus, it is instructive to move these states, with the methods discussed in Sec. IV E, and examine the cross section. For elastic scattering this is demonstrated in Fig. 17. Although it is difficult to draw any definite conclusions, this comparison supports the earlier arguments [74], showing lack of evidence for the low-lying 1_2^+ and 0_1^+ states. It should be noted that the 2^- resonance, suggested to be at around 3.5 MeV [74], may account for some discrepancy. As discussed in Ref. [22], the inelastic cross section is more sensitive to the presence

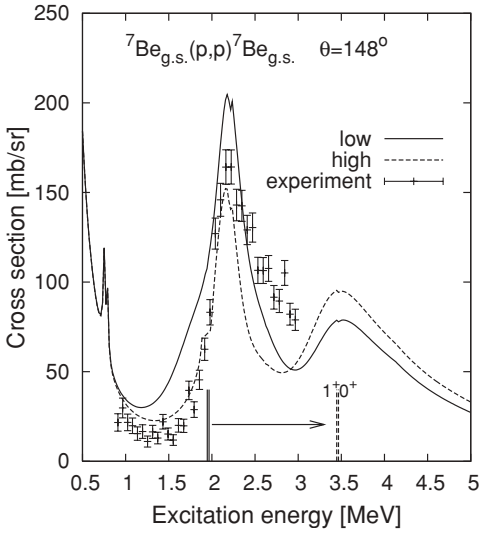

FIG. 17. Elastic differential cross section $^7\mathrm{Be}_{\mathrm{g.s.}}(p, p)^7\mathrm{Be}_{\mathrm{g.s.}}$ at $\theta = 148^\circ$ angle obtained with TDCSM. The solid line corresponds to the original position of the 1_2^+ and 0_1^+ (indicated by solid tick marks) states and the dashed line shows the cross section when both of these resonances are shifted up by 1.5 MeV. The shift is indicated with the arrow and the new positions of the states are marked with the dashed tick marks. Experimental data from Ref. [74] is included.

of the resonances in question. This cross section at $\theta = 148^\circ$ angle is shown in Fig. 18(a), where the solid line shows the original curve from Fig. 15, while the dashed line demonstrates the case when both states are moved up in energy by 1.5 MeV. Similar shift of the resonance positions is done in the R-matrix investigation in Fig. 18(b). From the figure it is evident that at

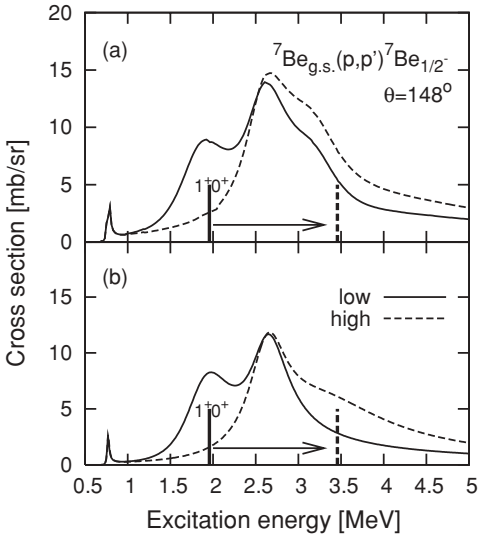

FIG. 18. Inelastic $^7\mathrm{Be}_{\mathrm{g.s.}}(p, p')^7\mathrm{Be}_{1/2^-}$ differential cross section at $\theta = 148^\circ$. Panel (a) form TDCSM and panel (b) from R-matrix calculations. In each case the solid line corresponds to the original position of 1_2^+ and 0_1^+ (indicated with solid tick marks) and the dashed line shows the cross section when both of these resonances are shifted up by 1.5 MeV. The shift is indicated with the arrow and the new positions of the states are marked with the dashed tick marks.

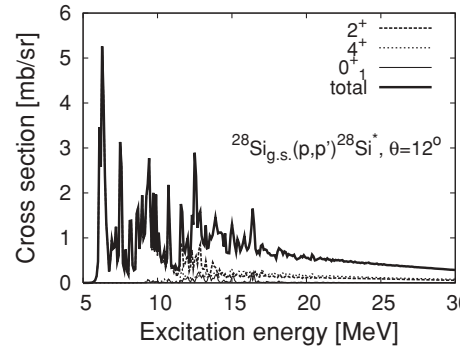

FIG. 19. Inelastic $^{28}\mathrm{Si}_{\mathrm{g.s.}}(p, p')^{28}\mathrm{Si}^*$ differential cross section at a $\theta = 12^\circ$ center-of-mass angle.

high energy the peaks associated with 1_2^+ and 0_1^+ become too broad to be observed. Hopefully, with the detailed theoretical predictions presented here, future experiments will resolve this controversy.

C. The ^{28}Si(p, p') reaction

As a final demonstration in Fig. 19 we show a large scale calculation for the $^{28}\mathrm{Si}(p, p')^{28}\mathrm{Si}^*$ reaction. This study is motivated by the ongoing experimental investigation of the (p, p') reactions in light nuclei, directed at the giant resonances and fine structure of the spectra. Here, we leave aside the problem of giant resonances and examine only the fine structure of complex reaction cross sections in the sd shell-model space. At low energies, up to 15 MeV of excitation, the contribution from the states with the particle-hole structure outside the sd shell is suppressed due to a low density of such states and difficulty in populating them in a single-particle reaction from the ground state of ^{28}Si. The results in Fig. 19 show the differential cross section at 12° center-of-mass angle used in the experiments. To stress the power of TDCSM approach, this continuum calculation includes over 80,000 resonant many-body states in ^{29}P, so that the direct matrix inversion is impossible, there are 132 channels, corresponding to the 14 lowest states in ^{28}Si. All of the final states up to 6_1^+ at 8543.56 keV are identified experimentally with the sd model space and the channel thresholds are adjusted correspondingly to reproduce the reaction kinematics. The discussion of this reaction is to be conducted on completion of the experimental investigations.

VI. CONCLUSIONS

A new time-dependent approach to the continuum shell model is presented in this article. This method takes its roots in the well-established Feshbach projection formalism and overcomes numerous difficulties, ranging from obtaining observables and treatment of self-energies to computational limitations of the many-body reaction physics and numerical stability for broad and narrow resonances. The large scope of this articles and many applications demonstrated here

emphasize the broad capability and versatility of the time-dependent approach.

We demonstrate the time evolution of many-body states, highlighting the complexity and nonexponential nature of the process. Illustrations combining chaotic and collective many-body dynamics with electromagnetic and particle decays are presented. While addressing the center-of-mass problem and its solution in the TDCSM, we show the effectiveness of the underlying time-dependent Green's function techniques. The realistic application to unbound states in oxygen exemplifies the renormalization of the Hamiltonian due to the interactions with continuum; these contributions improve the traditional SM approach and position the resonant states in agreement with the experimental observation. The TDCSM is presented in full readiness for the analysis of experiments, capturing the best from the traditional SM and uniting the structural features with reaction techniques. Adjustments of the interactions, positioning of the resonances, and incorporation of the interference features into the reaction physics are demonstrated. An in-depth comparison with R-matrix techniques are presented, revealing both consistency and superiority of the TDCSM. For the purpose of this comparison the controversial example of ^{8}B is selected with the interaction Hamiltonian that, as suggested in Refs. [22,24], produces several low-lying states, the position of which have been disputed. With the TDCSM approach the interpretation of the experimental data can be taken to a level beyond the position of peaks and their spectroscopic factors. As demonstrated with the case of ^{8}B, the angular distribution of the cross section has a strong dependence on the structure of many-body states and on the phases of individual components, thus providing for a direct experimental test of the underlying theoretical assumptions.

This article is built on realistic applications, all of them being inspired by different experiments of present-day interest. This is done to establish the broad applicability of the TDCSM and to demonstrate valuable capabilities and features that include effective handling of large model spaces with hundreds of different continuum channels, inclusion of Coulomb phases, extraction of full angular-momentum behavior, and the possibility of adjusting the interactions. It is the author's hope that the time-dependent approach to the continuum shell model, introduced here, will take its place among the most powerful and practical modern techniques unifying the many-body physics of structure and reactions.

ACKNOWLEDGMENTS

This work would not have been possible without the help and support from the members of the Nuclear Physics group at Florida State University. Most of all I wish to thank Grigory Rogachev for sharing his expertise in reaction physics and in R-matrix techniques. Meticulous comments from Don Robson helped overcome the most difficult theoretical issues. I am indebted to C. Hoffman, P. von Neumann-Cosel, G. Rogachev, S. Tabor, and I. Wiedenhöver; their experiments and related questions served as a fertile ground for this theoretical work. I am thankful to my teacher and friend Vladimir Zelevinsky; our earlier collaboration on the related topics constitutes a solid foundation for the development of new ideas presented here. The continued support from the US Department of Energy, grant DE-FG02-92ER40750, is recognized with gratitude.

APPENDIX A: CHANNEL AMPLITUDES

As it was said in Sec. II A, the terms $W(E)$ and $\Delta(E)$ are determined with the help of energy-dependent $\mathcal{P}$-space vectors $|A^c(E)\rangle$. Because the dynamics of the decay is usually driven by a simple coupling term in the interaction and the energy-dependent part is mostly determined by the kinematics, the many-body amplitude vector can be separated into two components $|A^c(E)\rangle = a^c(E)|c\rangle$. Here the amplitude $a^c(E)$ is the scalar function of energy and $|c\rangle$ is the energy-independent channel vector. In what follows we discuss amplitudes $a^c(E)$ for particle decays and electromagnetic transitions, the corresponding to these reactions channel vectors are addressed in Appendix B.

The decay amplitude for a single particle is determined by

$$a^c(\epsilon) = \sqrt{\frac{4\mu}{k}} \int_0^\infty dr\, F_l(kr)\, V_c(r)\, u_{\mathfrak{j}}(r), \tag{A1}$$

where $V_c(r)$ is a potential part of the Hamiltonian H for a particular channel c, which is modeled here by the Woods-Saxon shape, and $u_{\mathfrak{j}}(r)$ is a radial shell-model wave function. Fraktur font $\mathfrak{j}$ is used to denote a full set of single-particle quantum numbers; j, l, and s are among them. The F_l represents a regular continuum wave function given by either a Coulomb function, in case of a charged particle, or with a spherical Bessel function $F_l(kr) = krj_l(kr)$. The μ is the reduced mass and momentum is $k^2 = 2\mu\epsilon$, note that ϵ is the total energy E relative to the channel threshold. The channel label c includes single-particle quantum numbers; among them are angular momentum j and partial wave l. Equation (A1) can be viewed as a coordinate representation of Eq. (3) applied for a one-particle SM with a single intrinsic state $u_{\mathfrak{j}}(r)$.

For a neutral particle, near the decay threshold, namely at low kinetic energies, we have

$$F_l = (kr)^{l+1}/(2l+1)!! \propto \epsilon^{(l+1)/2}.$$

This together with Eq. (A1) results in the proportionality $a^c(\epsilon) = \varkappa\epsilon^{(l+1)/4}$, where the coefficient of proportionality $\varkappa$ is

$$\varkappa = \frac{\sqrt{2}(2\mu)^{(l+3/2)/2}}{(2l+1)!!} \int_0^\infty r^{l+1} V_c(r) u_{\mathfrak{j}}(r) dr.$$

This near-threshold behavior in Eq. (7) gives

$$\gamma_c(\epsilon) = \Theta(\epsilon)\varkappa^2\epsilon^{l+1/2} \text{ and } \Delta_c(\epsilon) = \frac{\varkappa^2}{2}\Theta(-\epsilon)\epsilon^l\sqrt{-\epsilon}, \tag{A2}$$

In Eq. (A2) $\Theta(\epsilon)$ is the Heaviside step function that assures proper consideration of $\epsilon = 0$ threshold, see also Refs. [14,31, 41].

The corresponding equations are well known in relation to the square well potential of radius R_c and the so-called Wigner

limit of the single-particle width [14,39]

$$\gamma_c(\epsilon) = \frac{2(kR_c)}{\mu R_c^2} \begin{cases} 1 & l = 0 \\ \frac{(kR_c)^{2l}}{[(2l-1)!!]^2}\left(\frac{2l-1}{2l+1}\right) & l \neq 0 \end{cases}.$$

Similar equations are available for the charged particles. The analytic expressions for the low-energy asymptotic of the Coulomb functions are more complicated [14,77]

$$F_l(kr,\eta) = \frac{(kr)^{l+1}}{(2l+1)!!}\frac{1}{l!}\sqrt{\frac{2\pi\eta}{e^{2\pi\eta}-1}\prod_{l'=1}^{l}(l'^2+\eta^2)}, \quad k \to 0.$$

For example, for $l = 0, s$ wave $F_0(kr,\eta) \sim (kr)\exp(-\pi\eta)$ leads to the decay amplitude $a^c(\epsilon) \sim \exp(-\pi\eta)$. This behavior is used to define an S factor

$$\mathcal{S} = \sigma(\epsilon)\epsilon\exp(2\pi\eta),$$

that unlike the cross section $\sigma(\epsilon)$ is constant in the low-energy limit.

It is possible to introduce an amplitude for the electromagnetic transitions, separating structural overlap from the energy dependence. The channel c is identified here with the type of transition (electric or magnetic), multipolarity L, and the final state I. The equation for the decay width, see Ref. [39], is

$$\Gamma_\alpha^c = |a^c(\epsilon)|^2 B(\mathrm{EM};\alpha \to c), \tag{A3}$$

where we define the amplitude as

$$|a^c(\epsilon)|^2 = \frac{8\pi(L+1)k^{2L+1}}{L[(2L+1)!!]^2}. \tag{A4}$$

Here k is the photon momentum that is proportional to its energy ϵ. The reduced electromagnetic transition rate $B(\mathrm{EM};\alpha \to c)$ is a structural overlap obtained from the energy-independent channel vector.

APPENDIX B: CHANNEL VECTORS

In what follows we discuss the energy-independent vector $|c\rangle$ from the full channel $|A^c(E)\rangle = a^c(E)\,|c\rangle$. This vector reflects the spectroscopic structure of the decay process. The channel vector belongs to the intrinsic $\mathcal{P}$ space. In addition to the total angular-momentum quantum number J, the channel label c carries information about the states of the decay products and their relative motion.

For a single-particle channel the channel vector includes the single-particle quantum numbers, among them are particle's spin s, information about the eigenstate $|I\rangle$ of the daughter nucleus with total spin I, and the partial wave quantum number l of the relative motion. These angular-momentum quantum numbers couple to the total channel spin J. For the following discussion we expand our notation for the channel vector by displaying its angular momentum J and by showing the intermediate angular-momentum couplings to the extent as needed. To be specific, a channel $|c\rangle = |c;J\rangle$ with the total angular momentum J in the j coupling scheme is expressed in full as $|c;\{\{ls\}_j, I\}_J\rangle$. Here the notation $\{ls\}_j$ stands for a spin-orbit coupling. The resulting single-particle momentum j together with the spin of the daughter nucleus I couple to the total angular momentum of the channel J.

In the standard j-scheme SM the channel vector for a single-particle decay is constructed by from the single-particle creation operator $a_j^\dagger$ acting on an eigenstate $|I\rangle$ of the daughter nucleus:

$$|c;\{jI\}_J\rangle = \{a_j^\dagger|I\rangle\}_J. \tag{B1}$$

The result is coupled to the total channel angular momentum J as indicated with brackets.

In the traditional SM approach, see perturbative treatment in Eqs. (8), (9), and (10), the overlap $C^2S = |\langle\alpha|c\rangle|^2$ between the channel vector and the eigenstate of the SM Hamiltonian α is known as the spectroscopic factor for the decay $\alpha \to c$. It is straightforward to check that definition (B1) is consistent with the standard textbooks, Ref. [39].

The normalization of the channel vectors is related to the occupation numbers $n_j(I) = \hat{j}\langle I|\{a_j^\dagger a_j\}_0|I\rangle$ of SM orbitals j in the state $|I\rangle$ of the daughter system:

$$\sum_J \hat{J}^2\,\langle c;\{jI\}_J|c;\{jI\}_J\rangle = \hat{I}^2[\hat{j}^2 - n_j(I)].$$

Here and in what follows we use $\hat{j} = \sqrt{2j+1}$.

The spin-channel representation is often used in the literature [4] because of its direct relation to the angular momentum of the projectile. In this representation the spin I of the target and spin s of the projectile are first coupled to the total spin S of the channel; the total angular momentum J is then a sum of S and l. The corresponding recoupling equations are

$$|c;\{l,\{Is\}_S\}_J\rangle = \sum_j (-1)^{l+s+I+J}\,\hat{j}\hat{S}\begin{Bmatrix} s & l & j \\ J & I & S \end{Bmatrix}|c;\{\{ls\}_j, I\}_J\rangle. \tag{B2}$$

The electromagnetic channels are constructed similarly:

$$|c;\{LI\}_J\rangle = \{\mathcal{M}_L|I\rangle\}_J,$$

where $\mathcal{M}_L$ is the electric or magnetic multipole operator, which is constructed from the particle-hole operators $\{a_j^\dagger a_{j'}\}_L$ as discussed in Ref. [39]. With this definition the electromagnetic transition rate is $B(\mathrm{EM};\alpha \to c) = |\langle\alpha|c\rangle|^2$, and together with the energy-dependent amplitude the decay width of a state is given by Eq. (A3).

APPENDIX C: DIFFERENTIAL CROSS SECTION

In this subsection we expand our discussion in Sec. II B and examine the procedure of the cross section calculation starting from the T-matrix. We consider reactions with unpolarized projectiles and targets, so the differential cross section is azimuthally symmetric and depends only on the zenith angle θ. We consider a general process $1 \to 2$ and subscripts 1 and 2 will denote quantities in the initial and final states, respectively. In most cases, apart from energy, initial and final states in an observed scattering process are identified with a target state of spin I and a projectile spin s.

It is convenient to start with a spin-channel representation and discuss independently the parts of the cross section that correspond to specific total S in the couplings $\{Is\}_S$ for initial and final states, S_1 and S_2. The angular dependence of the

cross section is expended via Legendre polynomials $P_L(\cos\theta)$ as [11,75]

$$\frac{d\sigma^{(1\to2)}}{d\Omega}(S_1, S_2) = \frac{1}{\hat{S}_1^2 k_1^2}\sum_L B_L^{(1\to2)}(S_1, S_2)P_L(\cos\theta), \quad \text{(C1)}$$

where Blatt-Biedenharn coefficients are

$$B_L^{(1\to2)}(S_1, S_2) = \frac{1}{4}\sum_{J_1 l_1 l_1'}\sum_{J_2 l_2 l_2'} Z_L(l_1 J l_1' J', S_1)Z_L(l_2 J l_2' J', S_2) \times \mathrm{Re}\left[\mathbf{T}^J_{l_2 S_2; l_1 S_1}\left(\mathbf{T}^{J'}_{l_2' S_2; l_1' S_1}\right)^*\right]. \quad \text{(C2)}$$

The matrix elements of the T-matrix in the channel space, Eq. (12), are denoted as

$$\mathbf{T}^J_{lS;l'S'} = \mathbf{T}_{cc'}, \quad \text{(C3)}$$

where the quantum numbers l and S for the spin-channel representation $|c\rangle = |c; \{l\{Is\}_S\}_J\rangle$ are explicitly shown in the subscript. The T-matrix is block diagonal due to the angular-momentum conservation $J = J'$; in the notation defined by Eq. (C3) the total angular momentum is indicated with a superscript. The angular-momentum recoupling coefficients are

$$Z_L(lJl'J', S) = (-)^{S+J}\hat{I}\hat{I}'\hat{J}\hat{J}'\begin{Bmatrix} l & J & S \\ J' & l' & L \end{Bmatrix}(l0, l'0|L0). \quad \text{(C4)}$$

The total, angle-integrated, cross section is

$$\sigma^{(1\to2)}(S_1, S_2) = \frac{\pi}{\hat{S}_1^2 k_1^2}\sum_J \hat{J}^2 \sum_{ll'}\left|\mathbf{T}^J_{l'S_2; lS_1}\right|^2. \quad \text{(C5)}$$

The j-coupling scheme is commonly used within the typical SM approach, it is also advantageous in work with single-particle reactions where Hamiltonian contains a spin-orbit interactions. By recoupling matrix elements (C3) with (B2) and after summation over all contributing spin-channels we obtain

$$\frac{d\sigma^{(1\to2)}}{d\Omega} = \frac{1}{\hat{s}_1^2\hat{I}_1^2 k_1^2}\sum_L B_L^{(1\to2)}P_L(\cos\theta), \quad \text{(C6)}$$

where the coefficients are

$$B_L^{(1\to2)} = \frac{1}{4}\sum_{\substack{j_1 j_2 l_1 l_2 J \\ j_1' j_2' l_1' l_2' J'}} A_L(\mathrm{j}_1\mathrm{j}_1'; I_1 J J')A_L(\mathrm{j}_2\mathrm{j}_2'; I_2 J J') \times \mathrm{Re}\left[\mathbf{T}^J_{I_2\mathrm{j}_2; I_1\mathrm{j}_1}\left(\mathbf{T}^{J'}_{I_2\mathrm{j}_2'; I_1\mathrm{j}_1'}\right)^*\right], \quad \text{(C7)}$$

with

$$A_L(\mathrm{j}\mathrm{j}'; IJJ') = \hat{J}\hat{J}'\hat{I}\hat{I}'\hat{\jmath}\hat{\jmath}'(-)^{I-s+J}\begin{Bmatrix} l & l' & L \\ j' & j & s \end{Bmatrix}\begin{Bmatrix} J & J' & L \\ j' & j & I \end{Bmatrix}(l0, l'0|L0).$$

Here j denotes a set of the single-particle quantum numbers $\{jls\}$, and the elements of the T-matrix $\mathbf{T}^J_{\mathrm{I}\mathrm{j};I'\mathrm{j}'} = \mathbf{T}_{cc'}$ are taken with channels in the j-coupling scheme $|c\rangle = |c; \{\{ls\}_j, I\}_J\rangle$. Eq. (C6) integrated over all angles gives total cross section in Eq. (14).

Scattering in the presence of Coulomb interactions is discussed in textbooks [12,14,41]. For pure Coulomb scattering the cross section is

$$\frac{d\sigma^C}{d\Omega} = |f^C(\theta)|^2, \quad \text{(C8)}$$

where the Coulomb amplitude is

$$f^C(\theta) = -\frac{\eta}{2k}\frac{1}{\sin^2(\theta/2)}\exp[-2i\{\eta\ln(\sin(\theta/2)) - \xi_0^C\}].$$

In general, for an elastic scattering process $(1 \to 1)$ of charged particles, a Coulomb phase $\xi_l^C = \arg[\Gamma(1 + l + i\eta)]$ in the channel with angular momentum l is to be inserted in Eq. (13). Moreover, the Coulomb effects are to be introduced in all partial waves that do not contribute to the nuclear interaction. The resulting total expression is a sum of the Coulomb cross section (C8), the nuclear cross section (C6), and an interference term. The interference part of the cross section is given by the same Eq. (C6), where different Blatt-Biedenharn coefficients

$$B_L^{\mathrm{I}} = -k\sum_{J\, j\, l=L}\hat{J}^2\,\mathrm{Re}\left\{\mathbf{T}^J_{\mathrm{I}j;Ij}e^{2i\xi_L}[f^C(\theta)]^*\right\} \quad \text{(C9)}$$

are to be used.

APPENDIX D: CHEBYSHEV POLYNOMIALS

The Chebyshev polynomials is a complete set of orthogonal polynomials $T_n(x)$, $n = 0, 1 \ldots \infty$, where both the domain of argument and the range of the function are in the $[-1, 1]$ interval. The Chebyshev polynomials can be defined via trigonometric relation

$$T_n[\cos(\theta)] = \cos(n\theta), \quad \text{(D1)}$$

the explicit polynomial expression is

$$T_n(x) = \frac{n}{2}\sum_{k=0,1,\ldots}^{k\leqslant n/2}\frac{(-1)^k}{n-k}\binom{n-k}{k}(2x)^{n-2k}. \quad \text{(D2)}$$

The Chebyshev polynomials form a complete and orthogonal set of functions on the interval $[-1, 1]$

$$\delta_{nm} = \frac{2-\delta_{n0}}{\pi}\int_{-1}^{1}\frac{T_n(x)T_m(x)}{\sqrt{1-x^2}}; \quad \text{(D3)}$$

they also form a complete and orthogonal set on the index space

$$\delta(x-y) = \sum_{n=0}^{\infty}\frac{2-\delta_{n0}}{\pi}\frac{T_n(x)T_n(y)}{\sqrt{1-x^2}}. \quad \text{(D4)}$$

The Chebyshev polynomials obey an "angular addition" identity that follows from the definition (D1)

$$2T_n(x)T_m(x) = T_{n+m}(x) + T_{n-m}(x), \quad n \geqslant m. \quad \text{(D5)}$$

The Chebyshev polynomials can be taken analytically onto a complex plane using definition

$$T_n(z) = \tfrac{1}{2}[(z+\sqrt{z^2-1})^n + (z-\sqrt{z^2-1})^n]. \quad \text{(D6)}$$

The Chebyshev polynomial diverge as n increases if argument is complex, this divergence can be regularized with complex

scaling. However, the technique based on the complex scaling is less numerically appealing because it cannot take a full advantage of the factorized nature of the terms that emerge due to the continuum coupling, see Sec. IV.

APPENDIX E: EVOLUTION OPERATOR EXPANSION

In summary of some of the earlier statements, the time-dependent approach allows for a numerically stable and computationally efficient treatment of many-body systems that feature both stable and unstable states. The success of the approach lies in its reflection of the underlying time-dependent, nonstationary physics. On the technical side, the method is iterative, based on the Hamiltonian matrix-vector multiplication, which is the most efficient operation available. Although there are many possibilities, the convergence properties are paramount. In a fixed number of iterations the desired precision at each point in time is to be reached, there is to be a defined cutoff at large times that corresponds to an energy resolution.

Not every representation of the evolution operator $\exp(-iHt)$ has these properties. For example Taylor expansion in powers of $\exp(-iHt) = \sum(-i)^n H^n t^n/n!$ is a rather poor approach. To attain a satisfactory energy resolution large times are to be considered, which requires extremely small terms $H^n/n!$ to be multiplied by the large t^n, and then summed with the oscillating signs; this leads to numerical instability. In the recent past expansions in orthogonal polynomial have been advertised as an alternative [42–44]. In particular, the Chebyshev polynomial expansion

$$\exp(-iHt) = \sum_{n=0}^{\infty} (-i)^n (2-\delta_{n0}) J_n(t)\, T_n(H), \qquad \text{(E1)}$$

appears to be effective. $J_n(t)$ in Eq. (E1) represents an n-th order Bessel function. The evaluation of the $T_n(H)|\lambda\rangle$ acting on any state λ can be done efficiently via recurrence relations. A finite SM Hamiltonian can be rescaled so that all eigenvalues lie within $[-1, 1]$; the polynomials then provide a good coverage of the region. There is a possibility to target a specific energy region, see Ref. [43]. Another important factor is that the expectation values of $T_n(H)$ do not go to zero for large n, so the construction of high-order polynomials can proceed as long as the errors propagated by the recurrence method are small.

Denoting $|\lambda_n\rangle = T_n(H)|\lambda\rangle$, we have the following iterative procedure for calculating $|\lambda_n\rangle$:

$$|\lambda_0\rangle = |\lambda\rangle, \quad |\lambda_1\rangle = H|\lambda\rangle, \quad \text{and}$$
$$|\lambda_{n+1}\rangle = 2H|\lambda_n\rangle - |\lambda_{n-1}\rangle. \qquad \text{(E2)}$$

With the (D5) property of the Chebyshev polynomials the expectation values for the Hermitian H are

$$\langle\lambda'|T_{n+m}(H)|\lambda\rangle = 2\langle\lambda'_m|\lambda_n\rangle - \langle\lambda'|\lambda_{n-m}\rangle, \quad n \geqslant m. \qquad \text{(E3)}$$

Below are some of the technical details, see also Ref. [43]. The spectrum of a the SM Hamiltonian is confined to a region $[E_{\min}, E_{\max}]$, where $E_{\min}$ and $E_{\max}$ can be taken as the smallest and the largest eigenvalues. Thus, the Green's function is to be mapped onto a generic interval $[-1, 1]$ by rescaling the Hamiltonian and selecting an energy scale $H \to (H - \overline{E})/\Delta E$ where $\overline{E} = (E_{\max} + E_{\min})/2$ and $\Delta E = (E_{\max} - E_{\min})/2$. With the energies bounded by $[-1, 1]$, the sampling time interval should be $\Delta t = \pi$. Given N (assume to be an even number) sampling points the time $t = \pi\tau$, where $\tau = 0 \ldots N-1$. With a discrete Fourier transform we obtain a set of energy points $E_p = p/(2N)$ with $p = -N/2 \ldots N/2$. The expectation value of the evolution operator in Eq. (17) at these discrete energies is

$$\langle\lambda'|G(E_p)|\lambda\rangle = -i\pi \left\{ \sum_{\tau=0}^{N-1} e^{2\pi i p\tau/N} \sum_{n=0}^{n_{\max}(\tau)} (-i)^n (2-\delta_{n0}) \times J_n(\pi\tau)\langle\lambda'|T_n(H)|\lambda\rangle \right\}. \qquad \text{(E4)}$$

The number of terms $n_{\max}(\tau)$ needed in the expansion of the evolution operator for each time τ is controlled by the asymptotic form of the Bessel function $J_n(x) \approx \sqrt{1/(2\pi n)}[ex/(2n)]^n$, requiring $n_{\max} > e\pi\tau/2$. It was found that $n_{\max}(\tau) = 4\tau$ or 30, whichever is larger, assures maximum numerical precision with minimal effort in computing the Chebyshev polynomials. The asymptote at fixed n but large times $J_n(t) \approx \sqrt{2/(\pi t)}\cos(t - \pi n/2 - \pi/4)$ ensures no divergences in the low-n terms at large time. Thus, to obtain N-energy points with the resolution of $2/N$ on the $[-1, 1]$ energy interval, $2N$ Hamiltonian-vector multiplications are required.

[1] T. Berggren, Nucl. Phys. **A109**, 265 (1968).
[2] U. Fano, Phys. Rev. **124**, 1866 (1961).
[3] G. Gamow, Z. Phys. **51**, 204 (1928).
[4] A. M. Lane and R. G. Thomas, Rev. Mod. Phys. **30**, 257 (1958).
[5] O. K. Rice, J. Chem. Phys. **1**, 375 (1933).
[6] T. Teichmann, Phys. Rev. **77**, 506 (1950).
[7] V. Weisskopf and E. Wigner, Z. Phys. **65**, 18 (1930).
[8] E. P. Wigner, Phys. Rev. **73**, 1002 (1948).
[9] P. A. M. Dirac and R. H. Dalitz, *The Collected Works of P.A.M. Dirac, 1924–1948* (Cambridge University Press, Cambridge/New York, 1995), see also Z. Phys. A **44**, 585 (1927).
[10] H. Feshbach, Ann. Phys. **5**, 357 (1958); **19**, 287 (1962).
[11] P. M. Endt, M. Demeur, and P. B. Smith, *Nuclear Reactions* (North-Holland, Amsterdam, 1959).
[12] H. Feshbach, *Theoretical Nuclear Physics: Nuclear Reactions* (Wiley, New York, 1991).
[13] C. Mahaux and H. A. Weidenmüller, *Shell-Model Approach to Nuclear Reactions* (North-Holland, Amsterdam/London, 1969).
[14] A. I. Baz, I. B. Zeldovich, and A. M. Perelomov, *Scattering, Reactions and Decay in Nonrelativistic Quantum Mechanics (Rasseyanie, reaktsii i raspady v nerelyativistskoi kvantovoi mekhanike)* (Israel Program for Scientific Translations, Jerusalem, 1969).
[15] M. L. Goldberger and K. M. Watson, *Collision Theory* (Wiley, New York, 1964).

[16] D. V. Savin, V. V. Sokolov, and H.-J. Sommers, Phys. Rev. E **67**, 026215 (2003).
[17] R. F. Barrett, B. A. Robson, and W. Tobocman, Rev. Mod. Phys. **55**, 155 (1983).
[18] A. M. Lane and D. Robson, Phys. Rev. **178**, 1715 (1969).
[19] A. M. Lane and D. Robson, Phys. Rev. **151**, 774 (1966).
[20] D. Robson and A. M. Lane, Phys. Rev. **161**, 982 (1967).
[21] A. M. Lane and D. Robson, Phys. Rev. **185**, 1403 (1969).
[22] D. Halderson, Phys. Rev. C **69**, 014609 (2004).
[23] D. Halderson, Int. J. Mod. Phys. E **14**, 171 (2005).
[24] D. Halderson, Phys. Rev. C **73**, 024612 (2006).
[25] R. J. Philpott, Nucl. Phys. **A289**, 109 (1977).
[26] K. Bennaceur, F. Nowacki, J. Okołowicz, and M. Płoszajczak, Nucl. Phys. **A651**, 289 (1999).
[27] J. Okołowicz, M. Płoszajczak, and I. Rotter, Phys. Rep. **374**, 271 (2003).
[28] I. Rotter, Rep. Prog. Phys. **54**, 635 (1991).
[29] A. Volya and V. Zelevinsky, Phys. Rev. C **67**, 054322 (2003).
[30] A. Volya and V. Zelevinsky, Phys. Rev. Lett. **94**, 052501 (2005).
[31] A. Volya and V. Zelevinsky, Phys. Rev. C **74**, 064314 (2006).
[32] S. Aoyama, T. Myo, K. Kato, and K. Ikeda, Prog. Theor. Phys. **116**, 1 (2006).
[33] N. Michel, W. Nazarewicz, M. Płoszajczak, and K. Bennaceur, Phys. Rev. Lett. **89**, 042502 (2002).
[34] N. Michel, W. Nazarewicz, M. Płoszajczak, and J. Okołowicz, Phys. Rev. C **67**, 054311 (2003).
[35] T. Myo, K. Kato, and K. Ikeda, Phys. Rev. C **76**, 054309 (2007).
[36] G. Hagen, D. J. Dean, M. Hjorth-Jensen, and T. Papenbrock, Phys. Lett. **B656**, 169 (2007).
[37] G. V. Rogachev, J. J. Kolata, A. S. Volya, F. D. Becchetti, Y. Chen, P. A. DeYoung, and J. Lupton, Phys. Rev. C **75**, 014603 (2007).
[38] N. Schwierz, I. Wiedenhöver, and A. Volya (2007), http://www.volya.com/ws, arXiv:0709.3525.
[39] A. Bohr and B. R. Mottelson, *Nuclear Structure I* (World Scientific, Singapore, 1998).
[40] P. von Brentano, Phys. Rep. **264**, 57 (1996).
[41] L. D. Landau and E. M. Lifshitz, *Quantum Mechanics: Non-Relativistic Theory* (Pergamon Press, New York, 1981).
[42] V. V. Dobrovitski and H. A. DeRaedt, Phys. Rev. E **67**, 056702 (2003).
[43] T. Ikegami and S. Iwata, J. Comput. Chem. **23**, 310 (2002).
[44] Y. L. Loh, S. N. Taraskin, and S. R. Elliott, Phys. Rev. E **63**, 056706 (2001).
[45] W. H. Press, S. A. Teukolsky, W. T. Vetterling, and B. P. Flannery, *Numerical Recipes in C++: The Art of Scientific Computing* (Cambridge University Press, Cambridge/New York, 2002).
[46] B. Giraud, Nucl. Phys. **71**, 373 (1965).
[47] T. Sebe, F. Khanna, and M. Harvey, Nucl. Phys. **A130**, 342 (1969).
[48] F. Palumbo, Nucl. Phys. **A99**, 100 (1967).
[49] R. D. Lawson, *Theory of the Nuclear Shell Model* (Clarendon Press, Oxford, 1980).
[50] B. A. Brown, Prog. Part. Nucl. Phys. **47**, 517 (2001).
[51] R. F. Barrett, L. C. Biedenharn, M. Danos, P. P. Delsanto, W. Greiner, and H. G. Wahsweiler, Rev. Mod. Phys. **45**, 44 (1973).
[52] L. Durand, Phys. Rev. D **14**, 3174 (1976).
[53] V. V. Sokolov and V. G. Zelevinsky, Nucl. Phys. **A504**, 562 (1989).
[54] S. Cohen and D. Kurath, Nucl. Phys. **A73**, 1 (1965).
[55] J. Stevenson, B. A. Brown, Y. Chen, J. Clayton, E. Kashy, D. Mikolas, J. Nolen, B. Samuel, B. Sherrill, J. S. Winfield *et al.*, Phys. Rev. C **37**, 2220 (1988).
[56] N. Ahsan and A. Volya, *Proceedings of the 9th International Spring Seminar on Nuclear Physics: Changing Facets of Nuclear Structure*, edited by A. Covello (World Scientific, Singapore, 2008), pp. 539–546.
[57] N. Michel, W. Nazarewicz, and M. Płoszajczak, Phys. Rev. C **75**, 031301(R) (2007).
[58] B. A. Brown, W. A. Richter, R. E. Julies, and B. H. Wildenthal, Ann. Phys. **182**, 191 (1988).
[59] A. G. Kofman and G. Kurizki, Nature **405**, 546 (2000).
[60] V. V. Flambaum and F. M. Izrailev, Phys. Rev. E **64**, 026124 (2001).
[61] E. Tryggestad, T. Baumann, P. Heckman, M. Thoennessen, T. Aumann, D. Bazin, Y. Blumenfeld, J. R. Beene, T. A. Lewis, D. C. Radford *et al.*, Phys. Rev. C **67**, 064309 (2003).
[62] P. von Brentano and M. Philipp, Phys. Lett. **B454**, 171 (1999).
[63] A. Volya and V. Zelevinsky, Nucl. Phys. **A788**, 251c (2007).
[64] V. V. Sokolov and V. G. Zelevinsky, Fizika (Zagreb) **22**, 303 (1990).
[65] N. Michel, W. Nazarewicz, and M. Płoszajczak, Nucl. Phys. **A794**, 29 (2007).
[66] C. Hoffman *et al.*, Phys. Lett. **B672**, 17 (2009).
[67] B. A. Brown and B. H. Wildenthal, Annu. Rev. Nucl. Part. Sci. **38**, 29 (1988).
[68] B. A. Brown and W. A. Richter, Phys. Rev. C **74**, 034315 (2006).
[69] A. Obertelli, S. Peru, J. P. Delaroche, A. Gillibert, M. Girod, and H. Goutte, Phys. Rev. C **71**, 024304 (2005).
[70] E. Khan, N. Sandulescu, M. Grasso, and N. V. Giai, Phys. Rev. C **66**, 024309 (2002).
[71] Y. Utsuno, T. Otsuka, T. Mizusaki, and M. Honma, Phys. Rev. C **60**, 054315 (1999).
[72] A. Csótó, Phys. Rev. C **61**, 024311 (2000).
[73] U. Greife, J. Livesay, C. Jewett, K. Chipps, F. Sarazin, D. Bardayan, J. Blackmon, C. Nesaraja, M. S. Smith, A. Champagne *et al.*, Nucl. Instrum. Methods B **261**, 1089 (2007).
[74] G. V. Rogachev, J. J. Kolata, F. D. Becchetti, P. A. DeYoung, M. Hencheck, K. Helland, J. D. Hinnefeld, B. Hughey, P. L. Jolivette, L. M. Kiessel *et al.*, Phys. Rev. C **64**, 061601(R) (2001).
[75] J. M. Blatt and L. C. Biedenharn, Rev. Mod. Phys. **24**, 258 (1952).
[76] F. C. Barker, Aust. J. Phys. **25**, 341 (1972).
[77] M. Abramowitz and I. A. Stegun, *Handbook of Mathematical Functions, with Formulas, Graphs, and Mathematical Tables* (Dover, New York, 1965).